

Potent and Selective Inhibitors of MTH1 Probe Its Role in Cancer Cell Survival

Jason G. Kettle,^{*,†} Husam Alwan,[†] Michal Bista,[‡] Jason Breed,^{||} Nichola L. Davies,[‡] Kay Eckersley,[§] Shaun Fillery,[‡] Kevin M. Foote,[‡] Louise Goodwin,[†] David R. Jones,[†] Helena Käck,[⊥] Alan Lau,[†] J. Willem M. Nissink,[‡] Jon Read,^{||} James S. Scott,[‡] Ben Taylor,^{||} Graeme Walker,[§] Lisa Wissler,[⊥] and Marta Wylot[‡]

[†]Oncology Innovative Medicines Unit, AstraZeneca, 35S47 Mereside, Alderley Park, Macclesfield, Cheshire SK10 4TG, United Kingdom

[‡]Oncology Innovative Medicines Unit, AstraZeneca, Unit 310, Darwin Building, Cambridge Science Park, Milton Road, Cambridge CB4 0WG, United Kingdom

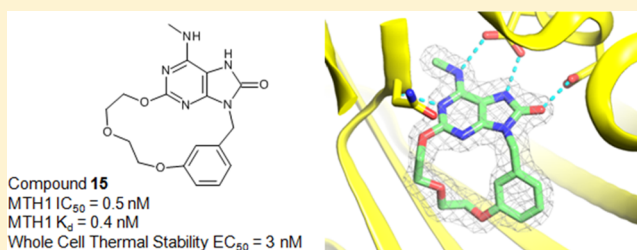
[§]Discovery Sciences, AstraZeneca, Mereside, Alderley Park, Macclesfield, Cheshire SK10 4TG, United Kingdom

^{||}Discovery Sciences, AstraZeneca, Unit 310, Darwin Building, Cambridge Science Park, Milton Road, Cambridge CB4 0WG, United Kingdom

[⊥]Discovery Sciences, AstraZeneca, Pepparedsleden 1, 431 83 Mölndal, Sweden

Supporting Information

ABSTRACT: Recent literature has claimed that inhibition of the enzyme MTH1 can eradicate cancer. MTH1 is one of the “housekeeping” enzymes that are responsible for hydrolyzing damaged nucleotides in cells and thus prevent them from being incorporated into DNA. We have developed orthogonal and chemically distinct tool compounds to those published in the literature to allow us to test the hypothesis that inhibition of MTH1 has wide applicability in the treatment of cancer. Here we present the work that led to the discovery of three structurally different series of MTH1 inhibitors with excellent potency, selectivity, and proven target engagement in cells. None of these compounds elicited the reported cellular phenotype, and additional siRNA and CRISPR experiments further support these observations. Critically, the difference between the responses of our highly selective inhibitors and published tool compounds suggests that the effect reported for the latter may be due to off-target cytotoxic effects. As a result, we conclude that the role of MTH1 in carcinogenesis and utility of its inhibition is yet to be established.



INTRODUCTION

Within the tumor cell, high levels of reactive oxygen species lead to oxidative damage of DNA directly, but damage may also occur to the free pool of nucleotides produced within the mitochondria. Such oxidative damage is believed to play a key role in spontaneous mutagenesis because incorporation of oxidized nucleotides into DNA can cause base-pair mistranslation, potentially leading to genomic instability and cell death. When incorporated in DNA, the oxidation product of dGTP, 8-oxo-dGTP, can be translated to an adenine rather than a cytosine moiety during replication, thereby leading to a transversion.¹ MTH1 is a member of the Nudix phosphohydrolase superfamily of enzymes and its role is to hydrolyze certain oxidized nucleotides, thereby preventing their incorporation into DNA, and its substrates include 8-oxo-dGTP and 2-OH-dATP. Recent papers claim a role for MTH1 in the general survival of cancer cells and describe experiments to support such a “cancer lethal” phenotype. Data are presented to show

that inhibiting MTH1 function either by RNAi-mediated knock-down of expression or by small molecule inhibition in vitro using novel compounds TH588 and TH287 (1 and 2),² or by *S*-crizotinib 3³ (Figure 1), the less active enantiomer of the clinically approved kinase inhibitor, leads to a cell killing effect in cancer but not nononcogenic cell lines, an effect which was associated with induction of enhanced DNA damage response. The authors tested their hypothesis using small molecule inhibitors and inducible shRNA in in vivo xenograft tumor models to show inhibition of tumor growth when targeting MTH1. Intrigued by these claims, we sought to repeat and extend the key validation work outlined and to develop novel independent chemical series with which to test the claimed effects of the compounds and target. If the role of MTH1 in tumor cell survival is as described then this would

Received: November 10, 2015

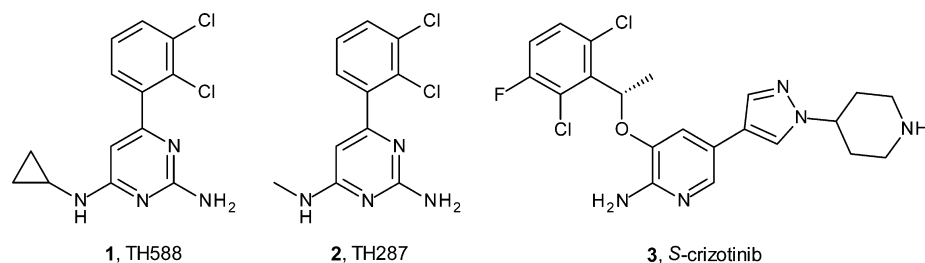


Figure 1. Literature inhibitors of MTH1, 1–3.

indeed be a highly significant discovery, although previous work in this area using MTH1(–/–) mice appeared somewhat contradictory.⁴ Fortunately, we had access to compounds that were able to serve as leads from a previous internal project that had sought agonists of Toll-like receptor 7 (TLR7) and established cross-reactivity with MTH1 as described below.

Toll-like receptors (TLR) are pattern recognition receptors that serve to recognize microbial pathogens and fragments of bacterial DNA in order to elicit an immune response.⁵ Such receptors are primed to recognize distinct pathogen-associated molecular patterns (PAMPs) within microbes. Imiquimod **4** (Figure 2), first developed by 3M Pharmaceuticals, is the only

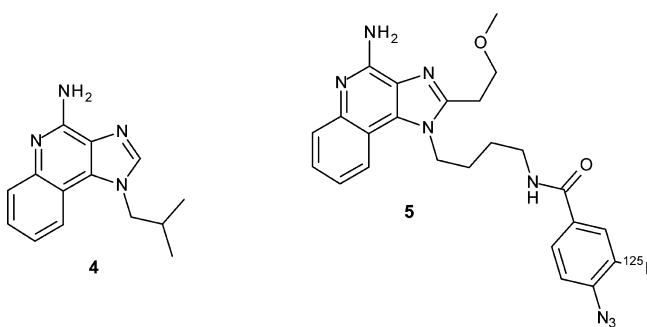


Figure 2. TLR7 agonist Imiquimod (**4**) and a photoaffinity probe TLR7 agonist (**5**).

approved small molecule agonist of toll-like receptor 7 (TLR7) and is used in the topical treatment of basal cell carcinoma (BCC), genital warts, and actinic keratosis. Agonism of TLR7 results in stimulation of the innate immune system via induction of cytokines such as interferon alpha (IFN α) and IL-12 and can result in significant antitumor activity. Clearance rates in BCC following imiquimod treatment have been reported in the range 73–87%, and for many patients the therapy is effectively curative.⁶ During the course of historical research into agonists of TLR7,⁷ a photoactivatable, cross-linkable TLR7 agonist probe based on an imiquimod template, **5** (pEC₅₀ of 1 μ M for the induction of IL-12 in THP-1 cells), was synthesized to identify which cellular proteins the probe interacted with. At the time of this research, such TLR7 agonists had not been shown to mediate their effects via a direct interaction with TLR7. Initial investigations were carried out on THP-1 cells as these could be differentiated to be TLR7 responsive. No displaceable binding was observed in a protein of molecular mass consistent with membrane associated TLR7, but displaceable binding was observed to a cytosolic 20 kDa protein. The interaction was observed in both differentiated and undifferentiated cells. This protein was determined to be MTH1. At this stage, a high-throughput screen was carried out against MTH1 with the intention of identifying additional novel

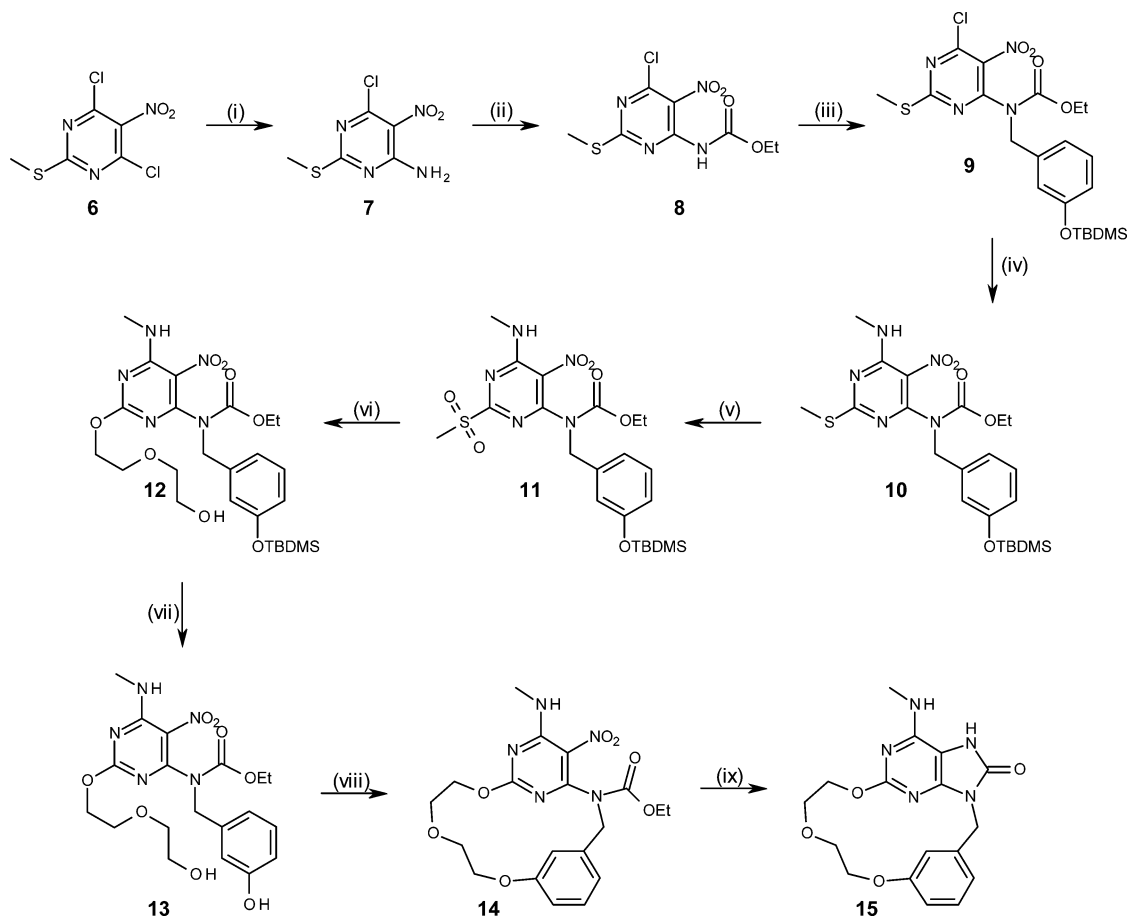
equity against this target and several series of interest were identified.

A working hypothesis that MTH1 may be the true effector of the efficacy of TLR7 agonists was ultimately discounted based on a number of key experiments, including the observation that TLR7 agonist activity was unaltered in splenocytes from MTH1 knockout mice and that an 85% reduction in protein expression of MTH1 via siRNA knock-down had no observable effect on TLR7 signaling. Intriguingly, further testing of TLR7 agonists from different chemical series also indicated cross-reactivity of these ligands with MTH1 and we speculate this may be due to recognition of the similar molecular architecture of the oxidized nucleotides that act as MTH1 substrates and the nucleotide bases present in the bacterial PAMPs.⁸ With the link to TLR7 disproven, internal research on MTH1 inhibitors was halted in 2003. When, more than a decade later, a role in oncology re-emerged for MTH1, this information proved crucial in enabling us to rapidly develop our own potent and selective cell probes with which to investigate this target as described below.

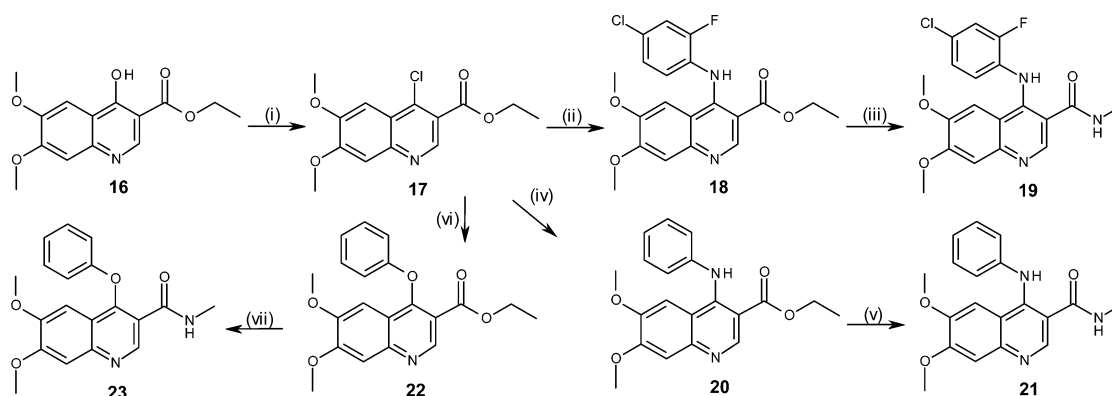
CHEMISTRY

The synthesis of macrocyclic MTH1 inhibitors followed closely the routes described for a related series of TLR7 agonists.⁹ Treatment of dichloropyrimidine **6** with ammonia gave aminopyrimidine **7**, which was protected as its ethylcarbamate derivative **8** in good yield (Scheme 1). Alkylation of the carbamate nitrogen with a protected phenolic benzyl group to give **9** was followed by displacement of the second chlorine atom to install the key methylamino motif in **10**. Introduction of the ether side chain to give **12** was achieved following displacement of the sulfone **11**, formed by oxidation of thioether **10**, with 2,2'-oxydiethanol. Removal of the *tert*-butyldimethylsilyl protecting group gave phenol **13**, which was subject to a Mitsunobu induced macrocyclization to give **14**. Finally, formation of the imidazolone ring was achieved by iron-mediated reduction of the nitro group with concomitant ring-closure onto the carbamate to give macrocycle **15**. An analogous strategy was adopted for lactams **30–33** (see Table 2), although in these cases the key macrocyclization step involved macrolactamization in place of Mitsunobu reaction (see Supporting Information).

Quinoline amides were constructed as shown in Scheme 2 from the 4-hydroxyquinoline ester **16** by conversion to the chloride **17** using phosphoryl trichloride then subsequent displacement with the requisite aniline, affording intermediates **18** and **20**. The ester functionality was then reacted with methylamine to give amide inhibitors **19** and **21**. Procedures for the synthesis of other members of this aniline series are described in the Supporting Information. The ether linked example was made by displacement of **17** with phenol under basic conditions and then hydrolysis of the ester **22**, conversion

Scheme 1. Synthesis of Macrocycle MTH1 Inhibitor 15^a

^aReagents and conditions: (i) NH_3 , *i*-PrOH, Et_3N , 0 °C, 5 h; (ii) EtOCOCl , THF, Et_3N , 0 °C, 5 h, 76% (2 steps); (iii) *m*-OTBDMS benzyl chloride, NaI, K_2CO_3 , acetone, 20 °C, 16 h; (iv) MeNH_2 , THF, 20 °C, 16 h, 100% (2 steps); (v) *m*CPBA, DCM, 20 °C, 2 h; (vi) 2,2'-oxididethanol, NaH, THF, 20 °C, 17 h, 71% (2 steps); (vii) TBAF, THF, 20 °C, 16 h, 86%; (viii) DTAD, Ph_3P , THF, 20 °C, 20 h, (ix) Fe, AcOH, water, 60 °C, 4 h, 7% (2 steps).

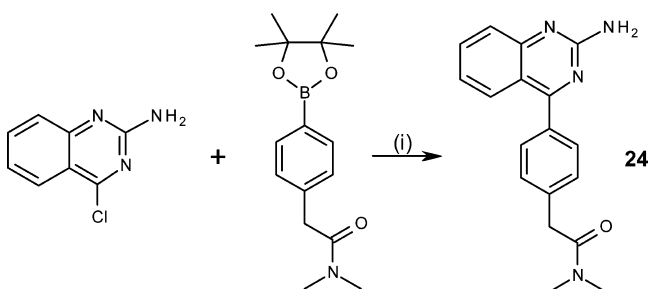
Scheme 2. Synthesis of Quinoline Amide MTH1 Inhibitors^a

^aReagents and conditions: (i) POCl_3 , 100 °C, 1 h, 90%; (ii) 4-chloro-2-fluoroaniline, AcOH, *i*-PrOH, 100 °C, 16 h, 99%; (iii) MeNH_2 , Me_3Al , THF, 60 °C, 2 h, 79%; (iv) aniline, AcOH, DMF, 100 °C, 1 h, 76%; (v) MeNH_2 , EtOH, 120 °C, 3 h, 81%; (vi) phenol, K_2CO_3 , MeCN, 80 °C, 16 h, 100%; (vii) (a) NaOH, THF, 20 °C, 17 h, (b) SOCl_2 , 80 °C, 1 h, (c) MeNH_2 , DMF/THF, 20 °C, 1 h, 74%.

to the acid chloride, and reaction with methylamine to give 23. Aminoquinazoline MTH1 inhibitor 24 was made using a Suzuki reaction between 4-chloroquinazolin-2-amine and phenyldimethylacetamide 4-boronic ester as shown in Scheme 3.

RESULTS AND DISCUSSION

Table 1 shows the MTH1 inhibitory potencies for a range of TLR7 modulators known in the literature. Imiquimod 4 itself has reasonable submicromolar potency, but Resiquimod, 25,¹⁰ known to be a much more potent TLR7 agonist, shows slightly

Scheme 3. Synthesis of Aminoquinazoline MTH1 Inhibitor 24^a

^aReagents and conditions: (i) Pd-118, K₂CO₃, 1,4-dioxane/H₂O, 100 °C, 2 h, 28%.

reduced affinity for MTH1. Compound **26** is from a distinct series of orally bioavailable purinone TLR7 agonists, first reported by Dainippon Sumitomo Pharmaceuticals,¹¹ that elicits a TLR7-mediated cellular response with similar potency to these clinical agents. Critical for this work, *N*-methylation of **26**, to give **27**, is observed to completely ablate TLR7 activity in this series and also results in a modest increase in MTH1 affinity. This observation has previously been reported for a closely related series of TLR7 agonist purinones and indicates that the exocyclic NH₂ motif is critical for TLR7 activity.¹² In a similar fashion, it has been reported that *N*-methylation of **4** also results in complete loss of TLR7 agonist activity.¹³ These data show that MTH1 is able to bind agonists of TLR7 as well as inactive close exemplars.

A crystal structure of compound **25** solved in complex with full length p18 isoform MTH1 (M1–156) with an N-terminal

6-His TEV protease cleavable tag is shown in Figure 3. Compound **25** (Figure 3a) makes hydrogen bonds between the

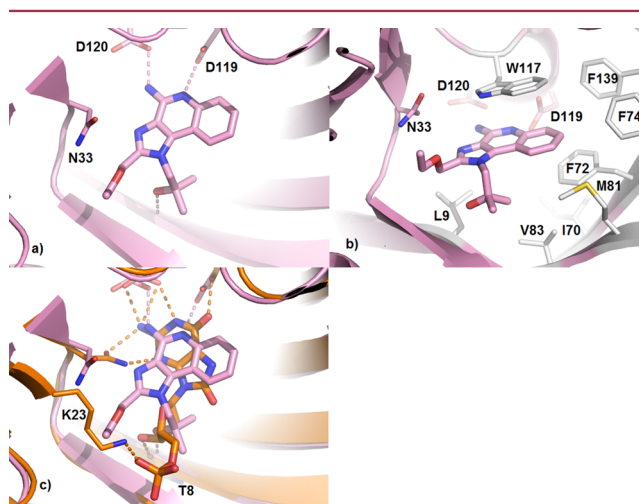


Figure 3. X-ray crystal structures of human MTH1 in complex with (a) **25** (pink, resiquimod), (b) complex with **25** rotated to show the hydrophobic residues (white), and (c) complexes with **25** and 8-oxo-dGMP (orange) superimposed. Selected carbon atoms, protein backbone cartoon, and close polar contacts are represented in the complex color. Compounds are shown as sticks, and protein residue side chains are shown as thinner sticks. Close polar contacts are represented as dotted lines.

quinoline nitrogen and residue D119 and the amino group and D120. These hydrogen bonds with D119 and D120 are common features of MTH1 ligands as demonstrated in the overlay with product 8-oxo-dGMP (Figure 3c) and also feature

Table 1. MTH1 Potencies of Assorted TLR7 Ligands^a

ID	Structure	MTH1 IC ₅₀ ¹	TLR7 mode of action	TLR7 EC ₅₀
4 Imiquimod		0.646	Agonist	NT
25 Resiquimod		2.056	Agonist	1.259 ²
26		2.809	Agonist	0.944 ²
27		0.536	Inactive	>100 ²

^{a1}Inhibition of MTH1 enzyme was assessed by detecting the inorganic pyrophosphate generated when the nucleoside triphosphate substrate, 8-oxo-dGTP, is hydrolyzed. ²Induction of IL-12 in human PBMC cells. All data are in μM and are the mean of at least *n* = 2 determinations and have SEM within 0.2 log units.

in protein–ligand structures of **1** and **3**. Compound **25** displays an additional hydrogen bonding contact with the backbone carbonyl of T8, another interaction it has in common with 8-oxo-dGMP (Figure 3c). The interaction with T8 is hypothesized to contribute to selectivity for the deoxyribose group of 8-oxo-dGMP.¹⁴ The dimethylhydroxy group of **25** pushes “down” into the pocket where the ribose of the substrate/product sits (Figure 3b and 3c). Two polar interactions made by the product 8-oxo-dGMP are not seen with inhibitors **25**; an interaction between the guanosine base and N33 and between the α -phosphate group and K23 terminal amino group. N33 is a mobile residue which can move to accommodate different chemotypes binding to MTH1. The quinoline ring of **25** occupies the same space as the nucleobase of 8-oxo-dGMP, nestling among a number of residues highlighted in Figure 3b. These residues form a pocket around the ligands making various hydrophobic and π -stacking interactions. The hydrophobic residues include W117 (above the purine binding site), L9, I70, F72, M81, and V83 (below the base binding site) and F74 and F139 (on the right-hand side of the nucleobase binding site). Finally, the side-chain of F27 is at the tip of a flexible loop (residues 23–31) that folds over the nucleobase binding site (not shown in Figure 1 for clarity). The mobility of this loop, along with minor shifts in other hydrophobic residues, readily accommodates different sizes and shapes of ligands. In the complex with **25**, rather unusually, the loop is open and the position that F27 normally adopts is occupied by a second molecule of **25**, which may be an artifact of the crystallographic system and high compound concentration used.

The X-ray crystal structure of compound **27** (Figure 4a) shows that it binds at the same site as compound **25** and the base of 8-oxo-dGTP, making the usual hydrogen bonding interactions with side chains of D119 and D120. The phenyl group binds in the hydrophobic site. The asparagine side chain of N33 moves in toward the binding site to occupy a similar conformation to that seen in the 8-oxo-dGMP complex. Examination of the crystal structure of **27** bound in MTH1 highlighted the relatively close proximity of the pendant methoxyethyl side chain to the N1-benzyl group, with the distance to the *meta*-position of the order of 3.5 Å (Figure 4a). We hypothesized that this close proximity of groups was unlikely to be a dominant conformation in solution, contributing to the moderate affinity observed. A macrocyclization strategy that connects the ether side chain to the *meta*-position of the benzyl group was expected to lock the molecule in its active binding conformation and result in significant potency gains through reduced entropic penalty of association and increased energy barrier of dissociation. Intriguingly, synthetic precedent for such a macrocyclization strategy had been reported in the patent literature for a series of purinone TLR7 agonists related to **26**.⁹ It is unclear given the lack of structural information for TLR7 how such a design strategy was arrived at, although homology models of TLR7 receptors have been reported.¹⁵

Gratifyingly, macrocyclization of **27** utilizing an *n*-pentyl bis-ether linker gave a compound with sub-nM potency against MTH1, **28**, representing over a 1700-fold increase in potency, validating our hypothesis around the relatively high energy binding conformation of the former (Table 2). This compound was relatively lipophilic, and so a contribution to this increase in potency from additional lipophilicity could not be ruled out (because compound **27** has a $\log D = 2.6$, **28** is nearly a log unit

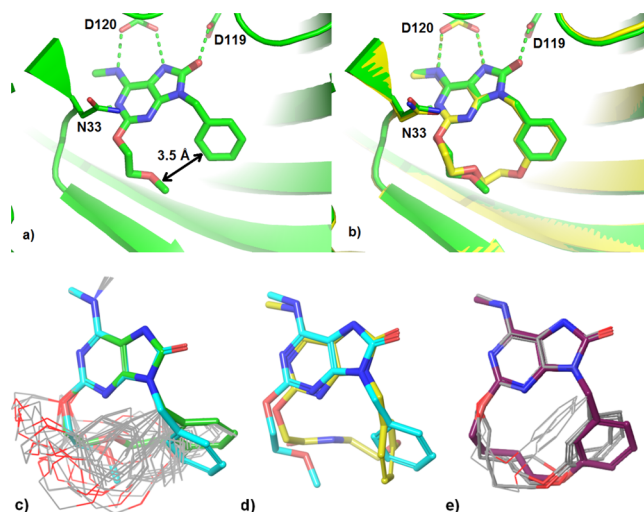


Figure 4. (a) X-ray crystal structures of human MTH1 in complex with **27** (green). (b) Complexes with **27** (green) and **15** (yellow) overlaid. Selected carbon atoms, protein backbone cartoon, and close polar contacts are represented in the complex color. Compounds are shown as sticks, and protein residue side chains are shown as thinner sticks. Close polar contacts are represented as dotted lines. Some atoms of the loop covering the active site (residues 23–31) have been removed for clarity. (c) Example conformational ensemble for **15**. Lowest-energy conformation (green) has a ring orientation similar to that seen for **27** (cyan) in the protein–ligand structure. (d) Modeled conformation of amide-containing macrocycle **30** (yellow) overlaid on X-ray structure conformation of **27** (cyan) shows differential orientation of phenyl ring. (e) Conformational ensemble of **29** derived using NMR suggests that the dominant conformations in solution (gray) are very similar to the conformation seen in the protein–ligand structure (maroon).

more lipophilic). One consequence of this increased lipophilicity is an increase in *in vitro* clearance as measured in human microsomes, although *in vitro* permeability is high and the compound demonstrates acceptable free binding levels in human plasma. Shortening the linker to an *n*-butyl bis-ether linker, compound **29**, gave a profile that was largely similar, but the reduced lipophilicity of this compound was not enough to improve *in vitro* clearance. A breakthrough came when introducing a polar ether linker into the all carbon side chain of **28** to give **15**. This compound maintained its exceptional potency against MTH1 but did so at lipophilicity less than that of the uncyclized analogue **27**, representing a 1000-fold increase in potency for no increase in $\log D$. With a reduction in $\log D$ came a significant improvement in *in vitro* clearance, with a profile comparable to **27**. Encouraged by this result, we sought to further improve properties by increasing the polarity of the linking group. Both secondary and tertiary amides **30** and **31** have substantially lowered $\log D$ ($= 1.3$), and this confers increased metabolic stability *in vitro*, together with high free levels. In each case, however, potency against MTH1 was compromised, as was permeability. The regioisomeric amides **32** and **33** were also synthesized, and the former at least demonstrated potent activity. Despite a $\log D$ of 1.8 for this compound, clearance remained very high, and indeed this compound proved to be unstable in human plasma. The tertiary amide analogue **33** had a similar profile but was substantially less active, more lipophilic, and similarly unstable in human plasma.

Table 2. MTH1 Potencies and in Vitro DMPK Profiles of Purinone Macrocycles^a

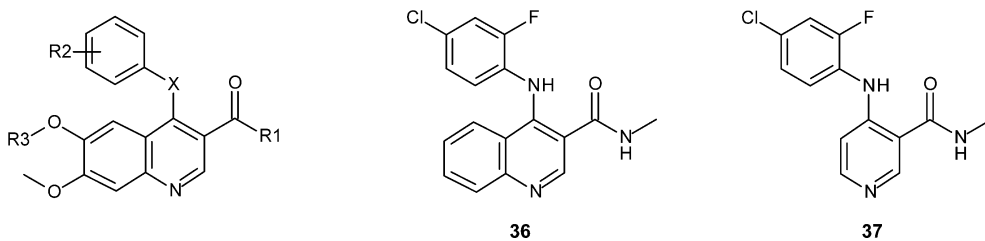
ID	Structure	MTH1 IC ₅₀ ¹	LogD ²	Clint Hu Mics ³	Hu PPB (% free) ⁴	Caco A-B ⁵	LLE ⁶
27		0.536	2.6	35	11	5.2	3.6
28		0.0003	3.5	186	1.9	8.2	6.1
29		0.0008	3.1	193	3.4	6.0	6.0
15		0.0005	2.4	48	7.7	3.2	6.9
30		0.153	1.3	11	41.5	<0.002	5.5
31		0.140	1.3	11	28.7	<0.003	5.6
32		0.0014	1.8	>300	unstable		7.1
33		0.888	3.0	>300	unstable		3.1

^a¹Inhibition of MTH1 enzyme was assessed by detecting the inorganic pyrophosphate generated when the nucleoside triphosphate substrate, 8-oxo-dGTP, is hydrolyzed. ²log *D* at pH_{7.4}. ³In vitro clearance in human microsomes (μL/min/mg). ⁴Percent free in human plasma. ⁵A to B permeability in Caco2 cells at pH_{7.4} (1 × 10⁻⁶ cm/s). ⁶LLE = pIC₅₀ - log *D*. All activity data are reported in μM and are the mean of at least *n* = 2 determinations and have SEM within 0.2 log units.

The SAR seen for the macrocycles is likely to be closely linked to their ability to adopt the correct conformation. Modeling suggests that macrocycles with linkers of 6 and 7 atoms are able to mimic the conformation of uncyclized analogue **27** in the binding pocket (Figure 4c) to varying degrees. Linkers shorter than six atoms were considered, but

their effect on conformation appeared more pronounced than with the longer linkers, and additionally, they proved less tractable chemically. Taking into account the difference in lipophilicity, the drop in potency between triether macrocycle **15** and amide-containing macrocycle **30** is approximately 30-fold. Conformational analysis of **30** showed that the preferred

Table 3. MTH1 Potencies and in Vitro DMPK Profiles of 3-Amidoquinolines



ID	R1	R2	R3	X	MTH1 IC ₅₀ ^a	log D ^b	Cl _{int} Hu Mics ^c	Hu PPB (% free) ^d	Sol (μM) ^e	LLE ^f
34	NH ₂	2-F, 4-Cl	Me	NH	0.0125	3.5	23	3.4	2	4.4
19	NHMe	2-F, 4-Cl	Me	NH	0.0009	3.3	13	3.9	15	5.7
35	NMe ₂	2-F, 4-Cl	Me	NH	1.22	2.5	13	6.6	6	3.4
36					0.002	3.3	6	6.2	8	5.5
37					0.009	3.1	10	8.9	39	4.9
21	NHMe	H	Me	NH	0.0005	2.7	14	9.1	108	6.6
38	NHMe	2-(CH ₂) ₂ SO ₂ Me	Me	NH	0.0005	1.7	8	22	30	7.6
23	NHMe	H	Me	O	5.75	2.1	13	14.7	35	3.1
39	NHMe	H	CH ₂ -4-N-Me-piperidine	NH	0.00008	1.6	8	51	>1000	8.4

^aInhibition of MTH1 enzyme was assessed by detecting the inorganic pyrophosphate generated when the nucleoside triphosphate substrate, 8-oxo-dGTP, is hydrolyzed. ^blog D at pH_{7.4}. ^cIn vitro clearance in human microsomes (μL/min/mg). ^dPercent free in human plasma. ^eAqueous solubility at pH_{7.4}. ^fLLE = pIC₅₀ - log D. All activity data are reported in μM and are the mean of at least *n* = 2 determinations and have SEM within 0.2 log units.

orientation of the phenyl of the amide macrocycle (Figure 4d) was different from the phenyl orientation seen for 27 and 15. However, a protein crystal structure of 30 (not shown) exhibits a phenyl orientation that is very similar to that of 27 and 15, and we hypothesize that the energetic cost of inducing this optimal orientation of the phenyl negatively affects the potency of 30. Such an effect is likely to play a role in the lower potency seen for 31 as well. The ligand-lipophilicity efficiency of alternative amide-containing macrocycle 32 and triether macrocycle 15 are similar, and comparison of their protein–ligand structures suggests that both are very similar in shape and conformation. The amide NH of 32 picks up an additional hydrogen bonding contact (not shown) to the backbone carbonyl of T8, but it is likely that the difference in potency between these compounds is largely caused by their difference in lipophilicity. Amide 33, an *N*-methylated analogue of 32, exhibits a markedly lower potency, which may be explained by abrogation of the amide hydrogen bond to T8 seen for 32 as well as conformational effects resulting from the *N*-methylation. The conformational hypothesis was corroborated by NMR experiments that showed unambiguously that conformations of the 6-linker compound 29 in solution closely resemble its modeled and protein-bound conformers (Figure 4c–e). NMR experiments on the nonmacrocylic precursor 27 did not yield a conformational ensemble, suggesting that the unlinked chain is very flexible.

In addition to the observations of cross-reactivity of TLR7 ligands with MTH1, the historical project also generated high-throughput screening data with the aim of identifying further chemical equity. Among the hits identified, a series of 3-amidoquinolines, exemplified by 19 and 34, stood out as worthy of further profiling (Table 3). Both primary amide 34 and secondary amide 19 had high potency against MTH1 (12.5 and 0.9 nM, respectively), but the dimethyl analogue 35 showed a significant loss of potency, providing a closely related compound with significantly less activity (>130-fold lower activity of 35 vs 19). The permeabilities of 19 and 35 as measured in a Caco-2 assay were high (P_{app} 24 × 10⁻⁶ and 33 ×

10⁻⁶ cm/s, respectively) with no evidence of efflux (efflux ratios of 0.5 and 0.6, respectively), giving confidence that the molecules penetrate into cells. Further exploration of secondary amide substitution (data not shown) showed no benefits in terms of potency or LLE, with methyl judged as being optimal. Deletion of both methoxy groups on the core gave 36 and led to a small potency decrease but with LLE and properties remaining similar. Further truncation of the quinoline to the pyridyl 37 somewhat surprisingly retained potency and showed some benefits in terms of solubility, although this remained a challenge for the series. The high potency of this fragment shows the tolerance of MTH1 for binding a diverse range of structural motifs, provided key pharmacophoric elements are met, and was suggestive of a high degree of substrate promiscuity.

The X-ray crystal structure of 19 in complex with MTH1 is shown in Figure 5. The compound occupies the same site as the base of 8-oxo-dGMP. Compound 19 makes the typical hydrogen bonds with D119 and D120, and the methoxy groups

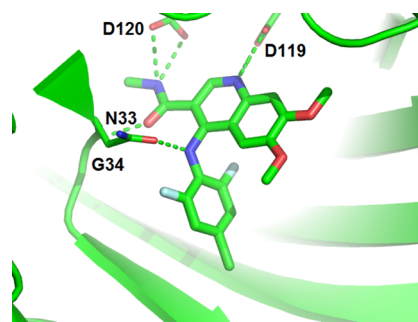


Figure 5. X-ray crystal structures of human MTH1 in complex with 19 (green). Selected carbon atoms, protein backbone cartoon, and close polar contacts are represented in the complex color. Compounds are shown as sticks, and protein residue side chains are shown as thinner sticks. Close polar contacts are represented as dotted lines. The 2-chloro-4-fluoro-phenyl group adopts a dual conformation.

sit among the hydrophobic residues. The side chain of N33 makes a hydrogen bond with the aniline nitrogen of **19**. The amide group makes an additional hydrogen bond with the backbone nitrogen of G34. A hit expansion library was carried out on lead **19** based on aniline substitution. Deletion of both halogens gave unsubstituted phenyl **21**, which was both more potent and less lipophilic, with improved LLE and physicochemical properties as a consequence. The permeability of **21** as measured in a Caco-2 assay was high (P_{app} 27×10^{-6} cm/s) with no evidence of efflux (efflux ratio 0.4) that could limit any cellular activity. The SAR showed a clear and consistent preference for ortho > meta > para substitution (based on six matched triplets, F, Cl, Me, CN, SO₂Me, and P(O)Me₂, data not shown). Introduction of polar substituents in the ortho position, exemplified by ethyl sulphone **38**, allowed further lowering of log *D* while increasing LLE. Importantly, switching the aniline to an aryl ether gave **23**, which reduced activity against MTH1 by >1000-fold relative to **19**, consistent with removal of a key interaction seen in the X-ray crystal structure. In an attempt to improve solubility in this series, we investigated addition of basic functionality at the 6-position as this looked most likely to be tolerated from inspection of the X-ray crystal structure. Bases such as **39** further enhanced potency (80 pM) and improved LLE (8.4), giving highly soluble, sub-nM inhibitors of MTH1.

A comparison of the rat pharmacokinetics of macrocycle **15**, in comparison to its uncyclized analogue **27**, is shown in Table 4. These data show a largely similar profile for the two

Table 4. Rat Pharmacokinetics of Macrocycle **15**, Its Uncyclized Analogue **27**, and Quinoline Amide **19**^a

ID	bioavailability (%)	clearance (mL/min/kg)	V _d _{ss} (L/kg)	t _{1/2} (h)
27	31	29	1.1	1.2
15	64	26	0.8	1.3
19	37	9	0.9	3.0

^aRat pharmacokinetics in Wistar Han rats followed a dose of 3 μMols/kg (po) and 1.5 μMols/kg (iv).

compounds, with increased bioavailability seen for the macrocycle suggestive of better permeability. Clearances are moderate, with a low volume of distribution typical of uncharged molecules. The moderate clearance and low volume combine to give a relatively short half-life of around 1 h in both

cases. It is clear that macrocyclization itself has had an overall neutral impact on the pharmacokinetic properties of this scaffold and a rather significant impact on potency at equivalent log *D*. The rat pharmacokinetics of quinoline **19** shows that the compound has low clearance and low volume, leading to a moderate half-life. Bioavailability of 37% is consistent with the reasonable solubility and high permeability of this compound as described above and is indicative of the potential of this series to develop tool compounds suitable for in vivo studies.

A third series of inhibitors based on a 2-aminoquinazoline template was also identified from the HTS, with hit **40** showing modest potency against MTH1 (Table 5). Dimethylation of the amine to give **41** resulted in reduced activity, while removal of the methyl (**42**) significantly increased potency against MTH1. A hit expansion library around **40** based on Suzuki couplings showed that *meta* and *para* substitution was favored over *ortho*. Transferring this SAR into the *des*-methyl series led to the identification of compounds such as dimethylamide **24** with enhanced MTH1 potency and acceptable physicochemical properties for further profiling. Permeability of **24** measured in a Caco-2 assay was high (P_{app} 34×10^{-6} cm/s) with no significant efflux (efflux ratio 0.7) that would limit cellular penetration. The X-ray crystal structure of **24** in complex with MTH1 is shown in Figure 6. The compound occupies the same

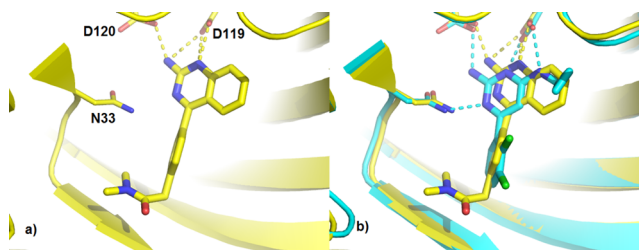
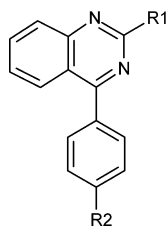


Figure 6. (a) X-ray crystal structures of human MTH1 in complex with **24** (yellow). (b) Complexes with **24** and **1** (PDB code: 4N1U, cyan) overlaid. Selected carbon atoms, protein backbone cartoon, and close polar contacts are represented in the complex color. Compounds are shown as sticks, and protein residue side chains are shown as thinner sticks. Close polar contacts are represented as dotted lines.

site as the base of 8-oxo-dGMP. An overlay of the complex of **24** with **1** (Figure 6a) shows that the aminopyrimidine rings of the two compounds make identical typical hydrogen bonds

Table 5. MTH1 Potencies and in Vitro DMPK Profiles of 2-Aminoquinazolines



ID	R1	R2	MTH1 IC ₅₀ ^a	log <i>D</i> ^b	Cl _{int} Hu Mics ^c	Hu PPB (% free) ^d	Sol (μM) ^e	LLE ^f
40	NHMe	H	3.32	3.6	215	0.9	7	1.9
41	NMe ₂	H	12.5	4.0	120	0.1	1	0.9
42	NH ₂	H	0.021	2.9	71	5.1	214	4.8
24	NH ₂	CH ₂ C(O)NMe ₂	0.009	2.0	5	4.1	118	6.1

^aInhibition of MTH1 enzyme was assessed by detecting the inorganic pyrophosphate generated when the nucleoside triphosphate substrate, 8-oxo-dGTP, is hydrolyzed. ^blog *D* at pH_{7.4}. ^cIn vitro clearance in human microsomes (μL/min/mg). ^dPercent free in human plasma. ^eAqueous solubility at pH_{7.4}. ^fLLE = pIC₅₀ - log *D*. All activity data are in μM and are the mean of at least *n* = 2 determinations and have SEM within 0.2 log units.

Table 6. Primary Target Potencies, Lipophilicity, and Selected Tumor Cell Line Antiproliferative Effects of MTH1 Inhibitors

ID	series	MTH1 IC ₅₀ ^a	MTH1 K _d ^b	MTH1 t _{1/2} (min) ^b	CETSA EC ₅₀ ^c	log D ^d	U2OS GI ₅₀ ^e	A549 GI ₅₀ ^e	H358 GI ₅₀ ^e	MCF7 GI ₅₀ ^f
1		0.003	0.005	3.9	0.010	3.5	3.0	3.3	2.3	4.0
3		0.138	0.039	0.1	3.6	2.2	2.2	3.8	4.9	4.4
27	TLR7	0.536	0.440		1.5	2.6				
28	macrocycle	0.0003	0.0002	151.7	0.009	3.5		12.1	29	8.2
15	macrocycle	0.0005	0.0004	81.2	0.003	2.4	>30	>30	>30	>30
19	quinoline	0.0009	0.0005	8.7	0.007	3.3	12.0	13.9	5.8	14.4
21	quinoline	0.0006	0.0002	3.5	NT	2.7	>30	>30	>30	>30
35	quinoline	1.22			0.95	2.5				
24	aminoquinazoline	0.009	0.003	2.1	0.080	2.0				

^aInhibition of MTH1 enzyme was assessed by detecting the inorganic pyrophosphate generated when the nucleoside triphosphate substrate, 8-oxo-dGTP, is hydrolyzed. ^bMTH1 affinity and half-life for dissociation as measured by surface plasmon resonance. ^cWhole cell thermal stability assay in K562 cells heated at 52 °C for 3 min. ^dlog D at pH_{7.4}. ^eGrowth inhibition in the indicated cell line following 5 day compound incubation. ^fGrowth inhibition in the indicated cell line following 7 day compound incubation. All activity data are in μM and are the mean of at least n = 2 determinations and have SEM within 0.2 log units.

with D119 and D120. The phenyl ring of the quinoline group sits in the same site as the cyclopropyl group among the hydrophobic residues of the nucleotide base binding pocket.

In addition to potent activity in an MTH1 enzyme assay, binding affinity for MTH1 protein was assessed independently by surface plasmon resonance (SPR) (Table 6). This data confirmed the high affinities seen and correlated well with potencies as measured in the biochemical assay, giving further confidence in the data. Intriguingly, observed half-lives for dissociation from MTH1 varied significantly according to chemotype. S-Crizotinib 3 showed rapid dissociation (t_{1/2} measured in seconds), whereas 1 and the quinazoline/quinoline scaffolds described here showed moderate half-lives (of the order of minutes). The macrocyclic inhibitors, however, showed significantly extended residence time with t_{1/2} in excess of 1 h for both 15 and 28 in contrast with acyclic precursors like 27, which dissociated rapidly (t_{1/2} in the range of seconds, beyond the resolution of SPR). On the basis of their high potencies and good permeability, examples from each series were assessed for their ability to penetrate cells and bind to MTH1 in a manner that was independent of a phenotypic end point. This is important because any phenotype which manifests itself predominantly as a cell killing effect as here may be particularly susceptible to any number of off-target effects that impact cell viability. For this, we utilized a whole cell thermal stabilization assay (CETSA)¹⁶ to assess target engagement in K562 cells, a technique that had also been employed for profiling of 1. In this assay, cells are treated with inhibitor and subject to small increases over a temperature gradient before cells are lysed and protein quantified by Western blot. Any compound binding to its target within the cell will have a stabilizing effect on, and prevent the thermal denaturation of, the protein relative to untreated cells. These primary melt curves and ligand-induced shifts are established to aid selection of testing conditions. The compound is then tested in increasing concentration at a single temperature to establish the CETSA EC₅₀ of target engagement. As can be seen in Table 6, the high enzymatic inhibitory activity of the macrocycles translated into very potent cellular target engagement with EC₅₀s of 9 and 3 nM for 28 and 15, respectively. These compared favorably with 1 for which in this assay we measure 10 nM (target engagement in this assay format is reported for this compound but potency is not disclosed). Nonmacrocylic analogue 27 has a much weaker in EC₅₀ of 1.5 μM, in line with its much reduced MTH1 enzyme activity. A similar observation

was made with the quinoline series, with 19 showing a potent CETSA EC₅₀ (7 nM) in marked contrast to dimethylated quinoline amide 35, which was less active in both the enzyme assay (IC₅₀ 1200 nM) and CETSA (EC₅₀ 950 nM) assays. The aminoquinazoline 24 showed an intermediate CETSA EC₅₀ (80 nM) in accordance with the lower MTH1 enzyme activity. Figure 7 shows the excellent correlation between MTH1

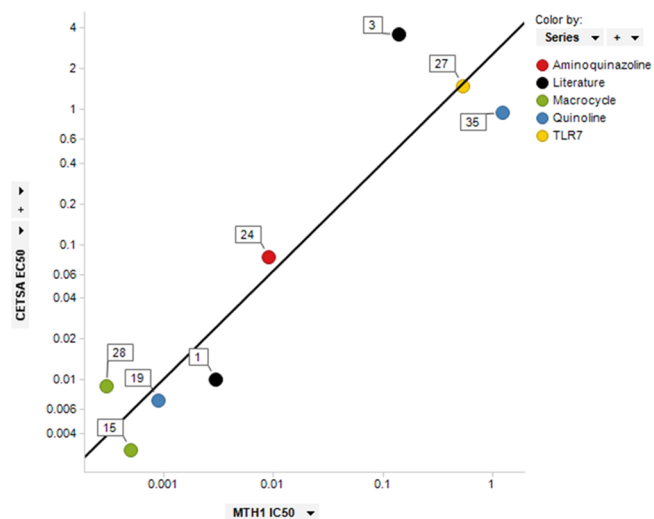


Figure 7. Correlation between MTH1 inhibitory potencies and target engagement in K562 cells colored by series. Straight line is line of fit.

inhibitory potency and measured target engagement in K562 cells, across each of these described series, together with 1 and 3. These data further support the conclusion that these diverse agents are potent, cell-active inhibitors of MTH1 function and highlight the value in pairing potent inhibitors with inactive or less active structurally related counterparts to act as negative controls in cell based experiments.

To further characterize the utility of these novel inhibitors, and to ensure any phenotype would not be confounded by off-target kinase inhibition, we profiled representative compounds 15, 19, 21, and 24 against an extended panel of kinases. Given the heritage of anilinoquinolines as kinase inhibitors, it was surprising to find that 15 did not show appreciable kinase inhibition at all (<35% at 10 μM across 267 kinases). Profiling of 19, 21, and 24 suggested no activity against any kinase at a testing concentration of 1 μM. In addition, these compounds

were profiled in a diverse panel of 153 secondary pharmacology targets and no notable off-target activities were observed that might confound phenotypic studies (these data are available as [Supporting Information](#)).

A selection of compounds was assessed for their ability to impact growth on a small panel of tumor cell lines (Table 6). Consistent with published data, **1** and **3** displayed modest but consistent growth inhibition in the range 3–5 μM , even though in our hands **3** exhibits relatively weak cellular target engagement. Macrocycle **28** demonstrated much weaker activity in this panel but did have an effect on viability at the top concentrations tested. Critically, however, macrocycle **15**, which is significantly less lipophilic than **28**, and has equivalent MTH1 potency, had no impact on cell viability. In a similar fashion, initial lipophilic quinoline screening hit **19** had modest antiproliferative effects. However, lowering its lipophilicity, as in example **21**, resulted in a compound which had no such impact on cell viability for equivalent potency. These assays used an extended 5- and 7-day compound incubation, although no further changes in potency were observed when compared to more typical 3-day incubation. We conclude that the modest effects observed with **19** and **28** are due to their increased lipophilicity and represent off-target, nonspecific, and MTH1-independent effects on cell growth. Analogue **15**, in a more acceptable lipophilicity range, shows potent engagement with MTH1 in cells and yet has no effect on cell viability (analogue **21** similarly has no impact on viability). These observations were also seen across much larger cell panels. Macrocycle **28**, despite showing some activity at high concentration in this mini-panel, was largely inactive in a wider panel of 212 tumor cell lines representing a diverse array of primary cancers. From this panel, 182 of 212 lines showed no impact on growth at all, and of those where a GI_{50} was determined, the highest potency was 6.74 μM , nearly 750-fold weaker than its measured cellular target engagement of MTH1. Quinoline **21** was tested in a panel of 135 cell lines and was inactive in 134 of them ($\text{GI}_{50} > 30 \mu\text{M}$), showing weak activity ($\text{GI}_{50} = 27.16 \mu\text{M}$) in a single cell line. However, consistent with the effects reported in the original disclosures, in a panel of 210 cell lines, **1** displayed broad antiproliferative activity consistent with a general cytotoxicity: moderately potent effects on cell viability across nearly all lines tested. Of the 211 cell lines assayed, only 10 showed no activity, with a mean GI_{50} of 6.5 μM across the remaining 201 lines (range 1.5–26.4 μM). Testing of **3** gave a largely similar profile.

In addition to limited effects on cell viability, cellular responses were assessed for **19** (at a concentration of 10 μM) through Western blotting of DNA damage response (DDR), p53, and apoptotic markers after 24, 48, or 72 h continual exposure. Compound **19** did not show increases in any of the DDR signaling markers tested (p-Ser1981 ATM, p-Ser15 p53, γH2AX , pSer4/8 RPA), nor did we observe induction of caspase-3 mediated apoptosis (cleaved PARP1) in the manner reported for **1** and **2** (Figure 8). Consistent with the literature data, we did observe increased p-Ser15 p53, p-Ser1981 ATM (albeit weakly), and caspase-mediated apoptosis induction (as measured by appearance of cleaved PARP1) upon treatment of U2OS cells with high concentrations of **1** (10 μM). However, we did not detect increases in other typical DNA double-strand break signaling markers such as γH2AX or pSer4/8 RPA and, somewhat confusingly, we observed robust apoptotic induction at time points (24 h) that preceded the appearance of maximal p-Ser15 p53 or p-Ser1981 ATM induction (48 h). Although the

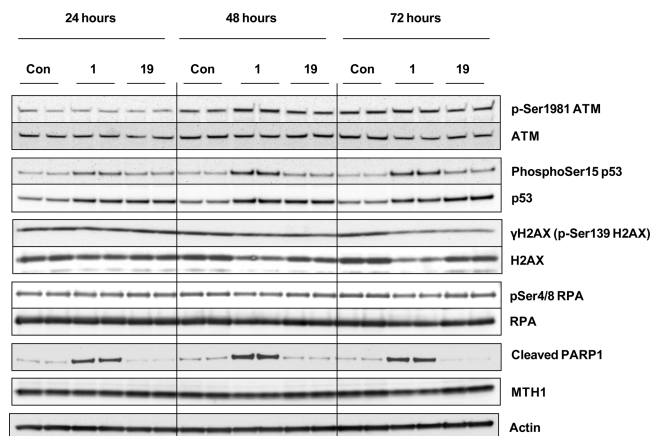


Figure 8. Induction of DDR signaling markers and apoptosis following treatment of U2OS cells for 24, 48, or 72 h with 10 μM **1** or **19**, compared to DMSO vehicle control (Con). Treatment with **1** leads to increased p-Ser1981 ATM, p-Ser15 p53 expression, and cleaved PARP1 (apoptosis). **19** shows no impact on DDR signaling activation or apoptosis. No changes in γH2AX or pSer4/8 RPA DDR signaling were observed for either compound.

mechanisms of apoptotic induction/cell death with **1** are unclear, the difference in DDR and apoptosis induction between compounds suggest that inhibition of MTH1 may not be sufficient to induce a meaningful DNA damage response.

Having observed key differences in effects on cell viability and DDR signaling for chemically diverse series of MTH1 inhibitors, we sought to revisit the genetic knockdown validation experiments disclosed in the original papers. Using a commercially available oligonucleotide targeting MTH1 that had a distinct sequence from those reported, we were able to induce complete silencing of MTH1, and yet this cell line was entirely viable, in stark contrast to the reported validation data (Figure 9a,b). Growth of this U2OS cell line was identical to that observed from one using a nontargeted siRNA and indicates that loss of MTH1 function is insufficient to affect cell viability. The original work detailed genetic ablation of protein using a sequence termed 'oligo #3'. We obtained this siRNA and repeated these experiments. In agreement with the data reported, using oligo #3 resulted in complete knockdown of MTH1 and a profound impact on cell viability. The observation that different siRNA can lead to knockdown of MTH1 protein expression but that only one leads to cell death is suggestive of off-target, nonspecific effects of the published siRNA. In our experience, such off-target liabilities of siRNA techniques, although well established,¹⁷ are not widely appreciated, and caution should be exercised when interpreting such results, particularly for end-points focused on cell death. In addition to siRNA knockdown experiments, we also generated CRISPR-mediated MTH1 knockout SW480 cell lines (Figure 9c,d). We were able to isolate multiple, stable cell clones that completely lack MTH1 expression. One such clone is shown in Figure 9: this clone grows as efficiently as its wild-type counterpart, further demonstrating MTH1 expression is not essential for cancer cell line viability.

Finally, in a further extension of the original validation work, we treated cell lines in which MTH1 had been knocked down with MTH1 inhibitors (Figure 10). Critically, **1** and **3** were each observed to kill cells that were MTH1-null, with potencies in line with those reported for endogenous tumor lines and

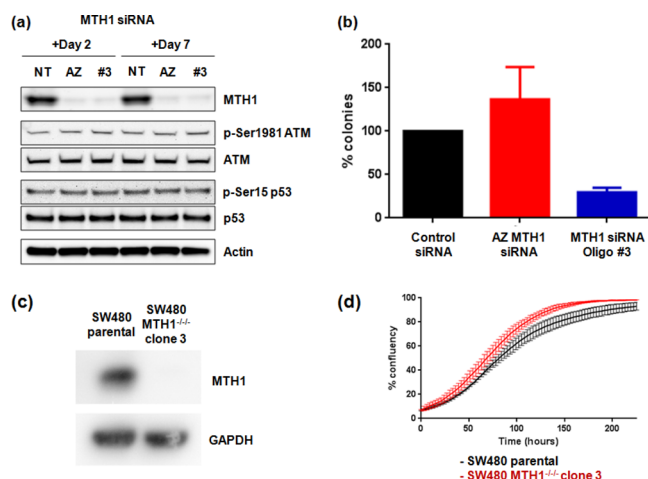


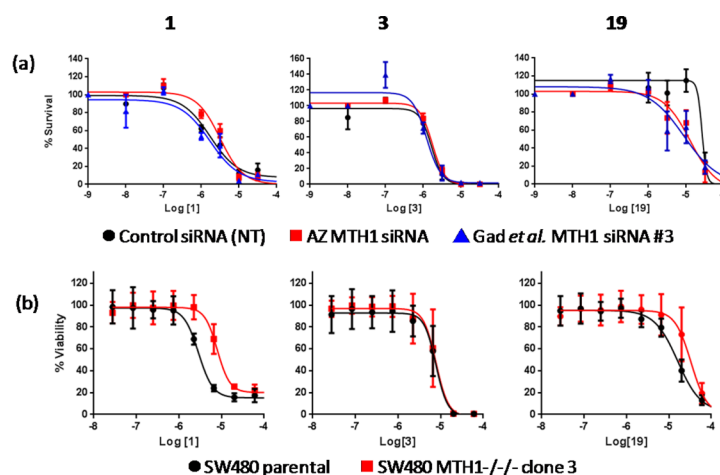
Figure 9. (a) Treatment of U2OS cells with siRNA to MTH1. Incubation for 2 and 7 days with both AZ and literature (#3) siRNA leads to significant knockdown of MTH1 protein relative to nontargeted (NT) controls, but no impact on other markers of DNA-damage response (DDR) activation as measured by *p*-Ser1981 ATM and *p*-Ser15 p53 expression. (b) MTH1 knockdown results in a significant reduction in clonogenic cell survival for literature (#3) siRNA but not a distinct AZ siRNA compared to control transfected cells. (c) Isogenic gene knockouts of MTH1 using CRISPR technology in SW480 cells. (d) Clones with complete knockout of all MTH1 alleles had undetectable levels of protein expression and were readily recoverable. Clones with complete knockout of MTH1 were not impaired in growth rate compared to SW480 parental cells.

with potencies that matched those lines treated with scrambled siRNA. Compound **19** similarly showed no separation between

these different genetic backgrounds. These experiments, which were not part of the original validation, indicate that the compounds cause cell death in an MTH1-independent manner, likely due to activity against unknown off-target mechanisms or general cytotoxicity. Consistent with this, the original validation experiments do highlight that MTH1 overexpression does not alter response to **3** and also that expression of the bacterial homologue of MTH1, MutT, could only partially rescue cells from the cytotoxic effects of **1** and **2**.

CONCLUSIONS

We have developed three distinct chemical series of MTH1 inhibitors to complement those recently described and to further probe the claimed role of this interesting enzyme. Critical to this was the knowledge this target had been tackled previously by AstraZeneca over a decade earlier. Although it may seem obvious, such continuity of information within a large organization should not automatically be assumed, not least because the original discoveries took place within a different disease-focused department, on a different site now no longer part of the AstraZeneca family, with data held on local drives in a nonsearchable format. In this instance, we relied on a small number of scientists who conducted the original programs, still present, to highlight knowledge that might easily have been lost or overlooked. In the work described herein, probes were developed through the strategies of (i) increasing potency of a weak hit through conformational restriction without increasing lipophilicity (**27** to **15**), (ii) reducing the lipophilicity of a potent inhibitor through atom deletion (**19** to **21**), or (iii) increasing potency while reducing lipophilicity through inclusion of polar functionality (**40** to **24**)



	1	3	19
Control siRNA (NT)	1.7	1.7	26.3
AZ MTH1 siRNA	3.2	1.7	12.8
Gad <i>et al.</i> MTH1 siRNA #3	1.7 (n=2)	1.2	8.7 (n=2)
SW480 parental	3.1	7.0	19.2
SW480 MTH1 ^{-/-} clone 3	8.4	7.2	34.3

Figure 10. MTH1 inhibitor cell viability is independent of MTH1. (a) Clonogenic survival of U2OS cells treated with **1**, **3**, or **19** following nontargeting control siRNA (NT), AZ MTH1 siRNA, or Gad *et al.* MTH1 siRNA #3. Values represent mean % of colonies forming \pm SD in comparison to nontargeting control siRNA treated cells from at least three independent experiments unless otherwise stated. (b) Viability of SW480 cell growth in parental and SW480 MTH1^{-/-} clone three cells treated with **1**, **3**, or **19**. Values represent mean % viability (CellTiter-Glo) relative to DMSO control-treated cells from at least five independent experiments \pm SD. Table: calculated GI₅₀ values in μ M for **1**, **3**, and **19** for experiments shown in (a) and (b).

as highlighted in Figure 11. It is not clear what the true target(s) of the published MTH1 inhibitors are that lead to the

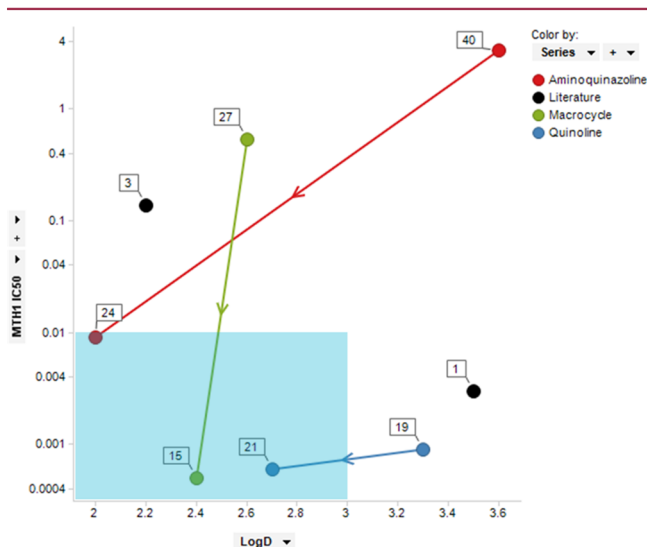


Figure 11. Plot of log *D* versus MTH1 enzyme potency for MTH1 inhibitors. Points are colored by chemical series, and arrows indicate the direction of optimization from screening hit to cell probe compound described in this study. The highlighted box is indicative of a potency and lipophilicity range deemed desirable for utility in probing target biology within cells in order to ensure potent and specific target modulation.

observed broad cell-killing effects, although it is possible that the mechanisms by which **1** and **3** achieve this are entirely different. High lipophilicity leading to general promiscuity is well documented¹⁸ and could be one such factor for **1**. Being the enantiomer of a marketed drug, **3** is in an acceptable property range, but its weaker activity, combined with its potential for additional off-target kinase activities, may contribute to the observed antiproliferative activity. Recent work highlights the value of tool compounds but also the associated pitfalls in choosing poorly characterized or promiscuous compounds with which to validate biology.¹⁹ The use of a photoaffinity probe based on **1**, in much the same way as is described here for TLR7 agonists, may be one way to dissect out the targets responsible for the antiproliferative activity in this series.

MTH1 inhibition has been proposed to “eradicate cancer” through a novel nononcogene addiction by targeting its function in hydrolyzing oxidized nucleotides, preventing their incorporation into DNA during replication and suppressing accumulation of otherwise lethal levels of DNA damage. However, it is not known at what level these oxidized nucleotides are expected to be lethal to cells (possibly due to an absence of reliable measures to quantify cellular levels of free oxidized nucleotides), therefore direct evidence linking MTH1 function and the consequences of their incorporation into the DNA in cancer cells remains to be understood. Indeed, deleting the bacterial MTH1 homologue or mouse MTH1 does not lead to cellular lethality despite the accumulation of thousands of mutations.²⁰ As the Nudix family of enzymes to which MTH1 belongs comprises more than 20 genes and other DDR pathways (e.g., base-excision repair) exist which repair oxidized bases in DNA, it is possible that redundancy may allow for cellular survival, a hypothesis that remains to be tested. In summary, our data using selective small molecule inhibitors,

siRNA knock-down, and CRISPR-mediated knockout of MTH1 does not support the claimed role of MTH1 being essential for cancer-cell survival.

EXPERIMENTAL METHODS

Chemistry. Unless otherwise stated, commercially available reagents were used as supplied. All reactions requiring anhydrous conditions were conducted in dried apparatus under an atmosphere of nitrogen. ¹H NMR spectra were recorded using a Bruker AV300 or AV400 NMR. Chemical shifts δ are reported in ppm, and multiplicity of signals are denoted s = singlet, d = doublet, t = triplet and m = multiplet, respectively. HRMS were recorded using a Shimadzu LCMS-2020 instrument (ESI+). Reactions and intermediates were also characterized by mass spectroscopy following liquid chromatography (LCMS or UPLC); purity of tested compounds was assessed to be at least 95% by UV using LCMS or UPLC analysis unless indicated otherwise. UPLC was carried out using a Waters UPLC fitted with Waters QDa mass spectrometer (column temp 40, UV = 190–400 nm, MS = ESI with pos/neg switching) at a flow rate of 1 mL/min using a solvent system of 95% A + 5% B to 5% A to 95% B over 8 min (total runtime with equilibration back to starting conditions was 10 min), where A = 0.1% formic acid or 0.05% TFA in water (for acid work) or 0.04% ammonia in water (for base work) B = acetonitrile. For acid or base analysis, the column used was Waters Acquity BEH 1.7 μ m, 2.1 mm \times 100 mm. LCMS was carried out using a Shimadzu UPLC fitted with a Shimadzu LCMS-2020 mass spectrometer and a Waters BEH C18 (50 mm \times 2.1 mm, 1.7 μ m) or Shim-pack XR-ODS (50 mm \times 3.0 mm, 2.2 μ m) or Phenomenex Gemini –NX 3 μ C18 110A (50 mm \times 3.0 mm, 3 μ m) column at a flow rate of 1.2 mL/min 95% A to 95% B over 2.0 min with a 0.6 min hold. Ion exchange purification was generally performed using a SCX-2 (Biotage, propylsulfonic acid functionalized silica, manufactured using a trifunctional silane, non-end-capped) cartridge. Column chromatography was performed on a Biotage system using a SiO₂ column with UV detection. Individual purification methods referred to here are detailed in the Supporting Information.

6-Chloro-2-(methylthio)-5-nitropyrimidin-4-amine (7). Ammonia in 2-propanol (27.1 mL, 54.2 mmol) was added dropwise to 4,6-dichloro-2-(methylthio)-5-nitropyrimidine **6** (10 g, 41.7 mmol) and triethylamine (8.7 mL, 62.5 mmol) in THF (200 mL) at –20 °C under nitrogen. The resulting mixture was stirred below 0 °C for 5 h. The solvent was removed under reduced pressure and the reaction mixture diluted with water (200 mL) and extracted with ethyl acetate (3 \times 200 mL). The organic layer was dried over Na₂SO₄, filtered, and evaporated to afford 6-chloro-2-(methylthio)-5-nitropyrimidin-4-amine (9.1 g, 99%) as a yellow solid. The product was used in the next step directly without further purification. ¹H NMR (DMSO-*d*₆, 300 MHz) δ 2.48 (3H, s), 8.11 (2H, s); *m/z* (ES+), [M + H]⁺ = 221; acidic, HPLC *t*_R = 1.023 min.

Ethyl (6-chloro-2-(methylthio)-5-nitropyrimidin-4-yl)carbamate (8). Ethyl carbonochloridate (4.7 g, 43.1 mmol) was added to 6-chloro-2-(methylthio)-5-nitropyrimidin-4-amine **7** (9.1 g, 41 mmol) and triethylamine (11.4 mL, 82 mmol) in THF (200 mL) at 0 °C under nitrogen. The resulting mixture was stirred at room temperature for 14 h. The reaction mixture was quenched with water (50 mL), extracted with ethyl acetate (3 \times 50 mL), and the organic layer dried over Na₂SO₄, filtered, and evaporated to afford a yellow solid. The crude product was purified by flash silica chromatography, elution gradient 0–15% ethyl acetate in petroleum ether. Pure fractions were evaporated to dryness to afford ethyl (6-chloro-2-(methylthio)-5-nitropyrimidin-4-yl)carbamate (9.2 g, 77%) as a pale-yellow solid. ¹H NMR (DMSO-*d*₆, 300 MHz) δ 1.21 (3H, t), 2.56 (3H, s), 4.14 (2H, q), 11.51 (1H, s); *m/z* (ES+), [M + H]⁺ = 293; acidic, HPLC *t*_R = 1.129 min.

3-((tert-Butyldimethylsilyloxy)benzaldehyde. *tert*-Butylchlorodimethylsilane (9.3 g, 61.4 mmol) was added portionwise to 3-hydroxybenzaldehyde (5 g, 40.9 mmol), triethylamine (11.4 mL, 81.9 mmol), and DMAP (0.25 g, 2.1 mmol) in DCM (100 mL) at room temperature. The resulting mixture was stirred at room temperature

for 2 h. The reaction mixture was diluted with DCM (500 mL) and washed sequentially with saturated aqueous ammonium chloride (150 mL \times 2) and saturated brine (200 mL \times 2). The organic layer was dried over Na_2SO_4 , filtered, and evaporated to afford 3-((*tert*-butyldimethylsilyloxy)benzaldehyde (11 g) as a pale-yellow oil. The product was used in the next step directly without further purification. ^1H NMR (chloroform-*d*, 300 MHz) δ 0.24 (6H, s), 1.01 (9H, s), 7.08–7.12 (1H, m), 7.30–7.54 (3H, m), 9.96 (1H, s); m/z (ES+), $[\text{M} + \text{MeCN}]^+ = 278$; acidic, HPLC $t_{\text{R}} = 1.835$ min.

3-((*tert*-Butyldimethylsilyloxy)phenyl)methanol. Sodium borohydride (0.77 g, 20.2 mmol) was added portionwise to 3-((*tert*-butyldimethylsilyloxy)benzaldehyde (11 g, 40.5 mmol) in methanol (100 mL) at 0 °C. The resulting mixture was stirred at 0 °C for 15 min. The solvent was removed under reduced pressure. The crude product was purified by flash silica chromatography, elution gradient 0–20% ethyl acetate in petroleum ether. Pure fractions were evaporated to dryness to afford 3-((*tert*-butyldimethylsilyloxy)phenyl)methanol (9.80 g) as a colorless oil which was used without further purification. ^1H NMR (chloroform-*d*, 300 MHz) δ 0.21 (6H, s), 0.96 (9H, s), 1.63–1.64 (1H, m), 4.65 (2H, s), 6.78 (1H, ddd), 6.87 (1H, s), 6.94 (1H, d), 7.22 (1H, dd); m/z (ES+), $[\text{M} + \text{H} - \text{H}_2\text{O}]^+ = 221$; acidic, HPLC $t_{\text{R}} = 1.297$ min.

***tert*-Butyl(3-(chloromethyl)phenoxy)dimethylsilane.** Thionyl chloride (4.6 mL, 62.9 mmol) was added to 3-((*tert*-butyldimethylsilyloxy)phenyl)methanol (10 g, 42 mmol) in DCM (150 mL) at 0 °C under nitrogen. The resulting mixture was stirred at room temperature for 5 h. The reaction mixture was quenched with ice water (100 mL) and extracted with DCM (2 \times 100 mL). The organic layer was washed sequentially with saturated NaHCO_3 (100 mL \times 3) and saturated brine (100 mL \times 2), and the organic layer dried over Na_2SO_4 , filtered, and evaporated to afford *tert*-butyl(3-(chloromethyl)phenoxy)dimethylsilane (10 g) as a colorless liquid. ^1H NMR (chloroform-*d*, 300 MHz) δ 0.21 (6H, s), 0.99 (9H, s), 4.53 (2H, s), 6.78 (1H, dd), 6.80 (1H, t), 6.97 (1H, dt), 7.21 (1H, t); m/z (ES+), $[\text{M} + \text{H}]^+ = 256$, GCMS $t_{\text{R}} = 8.350$ min.

Ethyl 3-((*tert*-Butyldimethylsilyloxy)benzyl(6-chloro-2-(methylthio)-5-nitropyrimidin-4-yl)carbamate (9). *tert*-Butyl(3-(chloromethyl)phenoxy)dimethylsilane (1.93 g, 7.5 mmol) was added to ethyl (6-chloro-2-(methylthio)-5-nitropyrimidin-4-yl)carbamate **8** (2 g, 6.8 mmol), sodium iodide (1 g, 6.8 mmol), and K_2CO_3 (1.42 g, 10.3 mmol) in acetone (40 mL) at 20 °C. The resulting mixture was stirred at room temperature for 16 h. The solid was filtered, and the solvent was removed under reduced pressure to afford crude ethyl 3-((*tert*-butyldimethylsilyloxy)benzyl(6-chloro-2-(methylthio)-5-nitropyrimidin-4-yl)carbamate (4 g, >100%) as a pale-yellow gum. The product was used in the next step directly without further purification; m/z (ES+), $[\text{M} + \text{H}]^+ = 513$; acidic, HPLC $t_{\text{R}} = 1.616$ min.

Ethyl 3-((*tert*-Butyldimethylsilyloxy)benzyl(6-(methylamino)-2-(methylthio)-5-nitropyrimidin-4-yl)carbamate (10). Methylamine (6.6 mL, 13.3 mmol) was added to ethyl 3-((*tert*-butyldimethylsilyloxy)benzyl(6-chloro-2-(methylthio)-5-nitropyrimidin-4-yl)carbamate **9** (4 g, 6.6 mmol) in THF (50 mL) at room temperature under nitrogen. The resulting mixture was stirred at room temperature for 16 h. The solvent was removed under reduced pressure, and the crude product was purified by flash silica chromatography, elution gradient 0–5% ethyl acetate in petroleum ether. Pure fractions were evaporated to dryness to afford ethyl 3-((*tert*-butyldimethylsilyloxy)benzyl(6-(methylamino)-2-(methylthio)-5-nitropyrimidin-4-yl)carbamate (3.1 g, 92%) as a yellow gum. ^1H NMR (chloroform-*d*, 300 MHz) δ 0.17 (6H, s), 0.96 (9H, s), 1.23 (3H, t), 2.47 (3H, s), 3.12 (3H, d), 4.15 (2H, q), 5.17 (2H, s), 6.71 (1H, dd), 6.91 (1H, d), 6.99 (1H, d), 7.15 (1H, t), 8.10 (1H, s); m/z (ES+), $[\text{M} + \text{H}]^+ = 508$; acidic, HPLC $t_{\text{R}} = 1.595$ min.

Ethyl 3-((*tert*-Butyldimethylsilyloxy)benzyl(6-(methylamino)-2-(methylsulfonyl)-5-nitropyrimidin-4-yl)carbamate (11). *m*CPBA (2.55 g, 14.8 mmol) was added to ethyl 3-((*tert*-butyldimethylsilyloxy)benzyl(6-(methylamino)-2-(methylthio)-5-nitropyrimidin-4-yl)carbamate **10** (3 g, 5.9 mmol) in DCM (40 mL) at room temperature. The resulting mixture was stirred at room temperature for 2 h. The

reaction mixture was diluted with DCM (100 mL) and washed sequentially with saturated aqueous NaHCO_3 (50 mL \times 3) and saturated brine (50 mL \times 2). The organic layer was dried over Na_2SO_4 , filtered, and evaporated to afford ethyl 3-((*tert*-butyldimethylsilyloxy)benzyl(6-(methylamino)-2-(methylsulfonyl)-5-nitropyrimidin-4-yl)carbamate (3.3 g, >100%) as a yellow gum. The product was used in the next step directly without further purification. ^1H NMR (chloroform-*d*, 300 MHz) δ 0.16 (6H, s), 0.95 (9H, s), 1.22 (3H, t), 3.14 (3H, s), 3.22 (3H, d), 4.21 (2H, q), 5.22 (2H, s), 6.71 (1H, ddd), 6.88 (1H, t), 6.96 (1H, d), 7.15 (1H, t), 7.93–8.10 (1H, m); m/z (ES+), $[\text{M} + \text{H}]^+ = 540$; acidic, HPLC $t_{\text{R}} = 1.398$ min.

Ethyl 3-((*tert*-Butyldimethylsilyloxy)benzyl(2-(2-(2-hydroxyethoxy)ethoxy)-6-(methylamino)-5-nitropyrimidin-4-yl)carbamate (12). Sodium hydride (0.73 g, 18.3 mmol) was added to 2,2'-oxidiethanol (3.89 g, 36.7 mmol) in THF (80 mL) at room temperature under nitrogen. The resulting mixture was stirred at room temperature for 1 h. Ethyl 3-((*tert*-butyldimethylsilyloxy)benzyl(6-(methylamino)-2-(methylsulfonyl)-5-nitropyrimidin-4-yl)carbamate **11** (3.3 g, 6.1 mmol) was added to the mixture, and the mixture was stirred at room temperature for 16 h. The reaction was quenched with saturated aqueous ammonium chloride (2 mL). The solvent was removed under reduced pressure and the crude product purified by flash silica chromatography, elution gradient 0–5% methanol in DCM. Pure fractions were evaporated to dryness to afford ethyl 3-((*tert*-butyldimethylsilyloxy)benzyl(2-(2-(2-hydroxyethoxy)ethoxy)-6-(methylamino)-5-nitropyrimidin-4-yl)carbamate (2.4 g, 69%) as a yellow gum. ^1H NMR (chloroform-*d*, 300 MHz) δ 0.16 (6H, s), 0.96 (9H, s), 1.19 (3H, t), 3.05–3.23 (3H, m), 3.56–3.68 (2H, m), 3.73–3.79 (4H, m), 4.17 (2H, q), 4.39–4.51 (2H, m), 5.17 (2H, s), 6.66–6.76 (1H, m), 6.87 (1H, m), 7.00 (1H, m), 7.14 (1H, td), 8.19 (1H, s), 1 \times OH not observed; m/z (ES+), $[\text{M} + \text{H}]^+ = 566$; acidic, HPLC $t_{\text{R}} = 1.365$ min.

Ethyl 3-Hydroxybenzyl(2-(2-(2-hydroxyethoxy)ethoxy)-6-(methylamino)-5-nitropyrimidin-4-yl)carbamate (13). TBAF in THF (5.1 mL, 5.1 mmol) was added to ethyl 3-((*tert*-butyldimethylsilyloxy)benzyl(2-(2-(2-hydroxyethoxy)ethoxy)-6-(methylamino)-5-nitropyrimidin-4-yl)carbamate **12** (2.4 g, 4.2 mmol) in THF (40 mL) at room temperature under nitrogen. The resulting solution was stirred at room temperature for 16 h. The reaction mixture was diluted with ethyl acetate (200 mL) and washed with saturated brine (50 mL \times 4). The organic layer was dried over Na_2SO_4 , filtered, and evaporated to afford crude product which was purified by flash C18-flash chromatography, elution gradient 0–60% methanol in water. Pure fractions were evaporated to dryness to afford ethyl 3-hydroxybenzyl(2-(2-(2-hydroxyethoxy)ethoxy)-6-(methylamino)-5-nitropyrimidin-4-yl)carbamate (1.64 g, 86%) as a yellow gum. ^1H NMR (DMSO-*d*₆, 400 MHz) δ 1.08 (3H, t), 2.97 (3H, d), 3.18 (1H, s), 3.43–3.50 (4H, m), 3.68 (2H, t), 4.04 (2H, q), 4.39 (2H, t), 5.01 (2H, s), 6.55–6.66 (1H, m), 6.72–6.81 (2H, m), 7.09 (1H, t), 8.62 (1H, broad d), 9.34 (1H, s); m/z (ES+), $[\text{M} + \text{H}]^+ = 452$; acidic, HPLC $t_{\text{R}} = 1.299$ min.

Ethyl 18-(Methylamino)-19-nitro-9,12,15-trioxa-2,17,20-triazatricyclo[14.3.1.1-4,8-]hencosa-1(20),4(21),5,7,16,18-hexaene-2-carboxylate (14). A solution of (*E*)-di-*tert*-butyl diazene 1,2-dicarboxylate (1.63 g, 7.1 mmol) in THF (20 mL) was added dropwise to a stirred solution of ethyl 3-hydroxybenzyl(2-(2-(2-hydroxyethoxy)ethoxy)-6-(methylamino)-5-nitropyrimidin-4-yl)carbamate **13** (1.6 g, 3.5 mmol) and triphenylphosphine (1.86 g, 7.1 mmol) in THF (120 mL) at room temperature under nitrogen. The resulting solution was stirred at room temperature for 20 h. The reaction mixture was quenched with water (2 mL). The solvent was removed under reduced pressure and the crude product purified by flash silica chromatography, elution gradient 0–100% DCM in petroleum ether. Pure fractions were evaporated to dryness to afford **14** (1.6 g, >100%) as a yellow oil which solidified on standing and was used in the next step without further purification; m/z (ES+), $[\text{M} + \text{H}]^+ = 434$; acidic, HPLC $t_{\text{R}} = 1.136$ min.

20-(Methylamino)-4,5,7,8-tetrahydro-15H-2,19-(azenometheno)-14,10-(methenonimidazo[5,1-*d*][1,2,15,3,5]-trioxadiazacycloheptadecin-17(18H)-one (15). Iron (2.22 g, 39.7 mmol) was added to **14** (1.6 g, 4 mmol) in acetic acid (16 mL) and

water (2 mL) at room temperature. The resulting mixture was stirred at 60 °C for 4 h. The reaction mixture was filtered through Celite and the solvent removed under reduced pressure. The crude product was purified by flash C18-flash chromatography, elution gradient 0–50% acetonitrile in water (containing 0.1% ammonia). Pure fractions were evaporated to dryness to afford **15** as a pale-yellow solid. This solid was purified by preparative HPLC (XSelect CSH Prep C18 OBD column, 5 μ silica, 19 mm diameter, 150 mm length), using decreasingly polar mixtures of water (containing 0.1% NH₄HCO₃) and acetonitrile as eluents. Fractions containing the desired compound were evaporated to dryness to afford **15** (0.1 g, 7%) as a white solid. ¹H NMR (700 MHz, DMSO) 2.88 (3H, d, *J* = 4.7 Hz), 3.58–3.60 (2H, m), 3.61–3.64 (2H, m), 4.01–4.05 (2H, m), 4.65–4.69 (2H, m), 4.82 (2H, s), 6.47–6.50 (1H, m), 6.77 (1H, dd, *J* = 2.1, 8.0 Hz), 6.95 (1H, d, *J* = 7.5 Hz), 7.16 (1H, t, *J* = 7.8 Hz), 7.74 (1H, 1H), 9.87 (1H, s); *m/z* (ES+), [M + H]⁺ = 358; base, HPLC *t_R* = 3.20 min. HRMS ESI+ *m/z* observed 358.1499, C₁₇H₂₀N₂O₄ requires 358.1515

Ethyl 4-Chloro-6,7-dimethoxyquinoline-3-carboxylate (17). Phosphoryl trichloride (150 mL, 59.9 mmol) was added to ethyl 4-hydroxy-6,7-dimethoxyquinoline-3-carboxylate **16** (16.6 g, 59.9 mmol). The resulting mixture was stirred at 100 °C for 1 h. The solvent was removed under reduced pressure, and the reaction mixture was adjusted to pH = 8 with saturated NaHCO₃ with ice bath cooling. The reaction mixture was filtered through Celite and the solid filtered then dried in an oven under reduced pressure to afford **17** (16 g, 90%) as a gray solid. ¹H NMR (DMSO-*d*₆, 300 MHz) δ 1.38 (3H, t), 3.97 (6H, s), 4.40 (2H, q), 7.50 (1H, s), 7.53 (1H, s), 8.97 (1H, s); *m/z* (ES+), [M + H]⁺ = 296; acid, HPLC *t_R* = 1.115 min.

Ethyl 4-((4-Chloro-2-fluorophenyl)amino)-6,7-dimethoxyquinoline-3-carboxylate (18). Acetic acid (3.1 mL, 54.1 mmol) was added to ethyl 4-chloro-6,7-dimethoxyquinoline-3-carboxylate **17** (4 g, 13.5 mmol) and 4-chloro-2-fluoroaniline (2.363 g, 16.23 mmol) in 2-propanol (60 mL) at room temperature under nitrogen. The resulting mixture was stirred at 100 °C for 16 h. The solvent was removed under reduced pressure, and the crude residue was triturated with ethyl acetate/diethyl ether to give a solid which was collected by filtration and dried under vacuum to give **18** (5.4 g, 99%) as a gray solid. ¹H NMR (DMSO-*d*₆, 300 MHz) δ 1.23 (3H, t), 3.63 (3H, s), 3.94 (3H, s), 4.11 (2H, q), 7.00 (1H, t), 7.13–7.24 (2H, m), 7.37 (1H, d), 7.42–7.60 (1H, m), 8.84 (1H, s), 9.42 (1H, s); *m/z* (ES+), [M + H]⁺ = 296; acidic, HPLC *t_R* = 1.0 min.

4-((4-Chloro-2-fluorophenyl)amino)-6,7-dimethoxy-N-methylquinoline-3-carboxamide (19). Trimethylaluminum (2 M in hexane) (3.7 mL, 7.4 mmol) was added to ethyl 4-((4-chloro-2-fluorophenyl)amino)-6,7-dimethoxyquinoline-3-carboxylate **18** (1.5 g, 3.7 mmol) and methylamine (2 M in THF, 5.56 mL, 11.1 mmol) in THF (20 mL) at room temperature. The resulting mixture was stirred at 60 °C for 2 h. The reaction mixture was poured into ice water (100 mL), diluted with DCM:methanol (10:1) (100 mL), and the mixture was stirred at room temperature for 15 min. The mixture was filtered through a Celite pad and washed with DCM:methanol (10:1) (100 mL), extracted with DCM:methanol (10:1) (3 \times 100 mL), and then the organic layer was dried over Na₂SO₄, filtered, and evaporated to afford a pale-yellow solid. The crude product was purified by flash C18-flash chromatography, elution gradient 0–70% acetonitrile in water (containing 0.05% ammonia). Pure fractions were evaporated to dryness to afford 4-((4-chloro-2-fluorophenyl)amino)-6,7-dimethoxy-N-methylquinoline-3-carboxamide **19** (1.14 g, 79%) as an off-white solid. ¹H NMR (400 MHz, DMSO) 2.66 (3H, d, *J* = 4.5 Hz), 3.61 (3H, s), 3.93 (3H, s), 6.82 (1H, t, *J* = 8.9 Hz), 7.06 (1H, s), 7.08–7.15 (1H, m), 7.34 (s, 1H), 7.46 (1H, dd, *J* = 2.2, 10.9 Hz), 8.61 (1H, d, *J* = 4.5 Hz), 8.73 (1H, s), 9.92 (1H, s); *m/z* (ES+), [M + H]⁺ = 390; acidic, HPLC *t_R* = 1.247 min. HRMS ESI+ *m/z* observed 390.1014, C₁₉H₁₈N₃O₃ClF requires 390.1021.

Ethyl 6,7-Dimethoxy-4-(phenylamino)quinoline-3-carboxylate (20). Acetic acid (0.097 mL, 1.7 mmol) was added to ethyl 4-chloro-6,7-dimethoxyquinoline-3-carboxylate **17** (1 g, 3.4 mmol) and aniline (0.37 mL, 4.1 mmol) in DMF (20 mL) at 25 °C. The resulting mixture was stirred at 100 °C for 1 h. The reaction was evaporated to dryness, and the crude product was purified by flash silica

chromatography, elution gradient 10–100% ethyl acetate (containing 2% triethylamine) in heptane. Pure fractions were evaporated to dryness to afford **20** (0.9 g, 76%) as a white solid. ¹H NMR (chloroform-*d*, 400 MHz) δ 1.45 (3H, t), 3.39 (3H, s), 4.00 (3H, s), 4.43 (2H, q), 6.86 (1H, s), 7.00–7.17 (3H, m), 7.22–7.41 (3H, m), 9.13 (1H, s), 10.31 (1H, s); *m/z* (ES+), [M + H]⁺ = 353.

6,7-Dimethoxy-N-methyl-4-(phenylamino)quinoline-3-carboxamide (21). Methylamine (33% in ethanol, 7.0 mL, 0.96 mmol) was added to ethyl 6,7-dimethoxy-4-(phenylamino)quinoline-3-carboxylate **20** (340 mg, 0.96 mmol) at 25 °C. The resulting mixture was stirred at 120 °C for 3 h. The reaction was evaporated and the crude product was purified by flash silica chromatography, elution gradient 0–15% methanol (containing 1% NH₄OH/methanol) in DCM. Pure fractions were evaporated to dryness, triturated with diethyl ether, and filtered to afford **21** (265 mg, 81%) as a cream solid. ¹H NMR (400 MHz, CDCl₃) 3.04 (3H, d, *J* = 4.8 Hz), 3.45 (3H, s), 4.00 (3H, s), 6.36 (1H, s), 6.90 (1H, s), 6.94–7.00 (2H, m), 7.03 (1H, t, *J* = 7.4 Hz), 7.25 (3H, d, *J* = 8.6 Hz), 8.70 (1H, s), 10.26 (1H, s); *m/z* (ES+), [M + H]⁺ = 338. HRMS ESI+ *m/z* observed 338.1492, C₁₉H₂₀N₃O₃ requires 338.1505

Ethyl 6,7-Dimethoxy-4-phenoxyquinoline-3-carboxylate (22). Potassium carbonate (140 mg, 1 mmol) was added to ethyl 4-chloro-6,7-dimethoxyquinoline-3-carboxylate **17** (150 mg, 0.5 mmol) and phenol (95 mg, 1 mmol) in acetonitrile (3 mL) at room temperature under nitrogen. The resulting mixture was stirred at 80 °C for 16 h. The solvent was removed under reduced pressure and the crude product was purified by flash silica chromatography, elution gradient 0–1% methanol in DCM. Pure fractions were evaporated to dryness to afford **22** (180 mg, 100%) as a pale-yellow gum. ¹H NMR (methanol-*d*₄, 300 MHz) δ 1.11 (3H, t), 3.82 (3H, s), 4.06 (3H, s), 4.14 (2H, q), 6.83–6.94 (2H, m), 7.07 (1H, t), 7.29–7.36 (3H, m), 7.47 (1H, s), 9.03 (1H, s); *m/z* (ES+), [M + H]⁺ = 354; acidic, HPLC *t_R* = 1.017 min.

6,7-Dimethoxy-N-methyl-4-phenoxyquinoline-3-carboxamide (23). NaOH (1.7 mL, 1.7 mmol) was added to ethyl 6,7-dimethoxy-4-phenoxyquinoline-3-carboxylate **22** (150 mg, 0.42 mmol) in THF (5 mL), and the resulting mixture was stirred at room temperature for 17 h. The reaction mixture was adjusted to pH = 6 with 2 M HCl, and then the solvent was removed under reduced pressure. The solid was collected by filtration then sulfurous dichloride (5 mL) was added and the mixture was stirred at 80 °C for 1 h. The solvent was removed under reduced pressure, and then the residue was dissolved in DMF (5 mL), methylamine (2 M in THF, 2.0 mL, 4.0 mmol) was added, and the mixture was stirred at room temperature for 1 h. The solvent was removed under reduced pressure and the crude product was purified by preparative HPLC (XSelect CSH Prep C18 OBD column, 5 μ silica, 19 mm diameter, 150 mm length), using decreasingly polar mixtures of water (containing 0.1% NH₄HCO₃) and acetonitrile as eluents. Fractions containing the desired compound were evaporated to dryness to afford **23** (92 mg, 74%) as a white solid. ¹H NMR (300 MHz, DMSO) 2.58 (3H, s), 3.74 (3H, s), 3.96 (3H, s), 6.90 (2H, d, *J* = 7.8 Hz), 7.07 (1H, t, *J* = 7.4 Hz), 7.16 (1H, s), 7.26–7.38 (2H, m), 7.48 (1H, s), 8.30 (1H, d, *J* = 4.6 Hz), 8.77 (1H, s); *m/z* (ES+), [M + H]⁺ = 339; acidic, HPLC *t_R* = 1.110 min. HRMS ESI+ *m/z* observed 339.1363, C₁₉H₁₉N₂O₄ requires 339.1345

2-(4-(2-Aminoquinazolin-4-yl)phenyl)-N,N-dimethylacetamide (24). Pd 118 (35 mg, 0.05 mmol) was added to *N,N*-dimethyl-2-(4-(4,4,5,5-tetramethyl-1,3,2-dioxaborolan-2-yl)phenyl)acetamide (435 mg, 1.5 mmol), potassium carbonate (139 mg, 1 mmol), and 4-chloroquinazolin-2-amine (180 mg, 1 mmol) in 1,4-dioxane (5 mL) and water at 25 °C under nitrogen. The resulting mixture was stirred at 100 °C for 2 h. The reaction was evaporated and the crude product was purified by flash silica chromatography, elution gradient 0–10% methanol in DCM. Pure fractions were evaporated to dryness and triturated with ether, filtered, and dried to afford **24** (85 mg, 28%) as a light-brown solid. ¹H NMR (400 MHz, CDCl₃) 3.00 (3H, s), 3.06 (3H, s), 3.83 (2H, s), 5.22 (2H, s), 7.22 (1H, ddd, *J* = 1.4, 6.7, 8.2 Hz), 7.45 (2H, d, *J* = 8.3 Hz), 7.62–7.66 (1H, m), 7.66–7.74 (3H, m), 7.83–7.9 (1H, m); *m/z* (ES+), [M + H]⁺ = 307. HRMS ESI+ *m/z* observed 307.1552, C₁₈H₁₉N₄O requires 307.1559.

■ ASSOCIATED CONTENT

Supporting Information

The Supporting Information is available free of charge on the ACS Publications website at DOI: 10.1021/acs.jmedchem.5b01760.

Protocols for the enzyme, SPR, NMR, and cell assays, synthetic methods for the remaining examples, together with crystallographic information, and kinase panel and secondary pharmacology selectivity data for compounds (PDF)

Molecular formula strings (CSV)

■ AUTHOR INFORMATION

Corresponding Author

*Phone: +44 (0)1625 517920. Fax: +44(0)1625519749. E-mail: jason.kettle@astrazeneca.com.

Notes

The authors declare no competing financial interest.

■ ACKNOWLEDGMENTS

We thank all past members of the original MTH1 program from AstraZeneca Charnwood without whom this work would not have been possible. We also thank David Whittaker, Calum Cook, David Perkins, and Scott Boyd for aspects of synthesis. We thank Pelago Bioscience for performing cellular thermal stability assays.

■ ABBREVIATIONS USED

BCC, basal cell carcinoma; CETSA, cellular thermal shift assay; CRISPR, clustered regularly interspaced short palindromic repeats; DDR, DNA-damage response; LLE, ligand-lipophilic efficiency; PAMPs, pathogen-associated molecular patterns; PBMC, peripheral blood mononuclear cells; SEM, standard error of means; SPR, surface plasmon resonance

■ REFERENCES

- Freudenthal, B. D.; Beard, W. A.; Perera, L.; Shock, D. D.; Kim, T.; Schlick, T.; Wilson, S. H. Uncovering the polymerase-induced cytotoxicity of an oxidized nucleotide. *Nature* **2015**, *517*, 635–639.
- Gad, H.; Koolmeister, T.; Jemth, A.-S.; Eshad, S.; Jacques, S. A.; Ström, C. E.; Svensson, L. M.; Schultz, N.; Lundbäck, T.; Einarsdóttir, B. O.; Saleh, A.; Göktürk, C.; Baranczewski, P.; Svensson, R.; Bernthsson, R. P.-A.; Gustafsson, R.; Strömberg, K.; Sanjiv, K.; Jacques-Cordonnier, M.-C.; Desroses, M.; Gustavsson, A.-L.; Olofsson, R.; Johansson, F.; Homan, E.-J.; Loseva, O.; Bräutigam, L.; Johansson, L.; Höglund, A.; Hagenkört, A.; Pham, T.; Altun, M.; Gaugaz, F. Z.; Vikingsson, S.; Evers, B.; Henriksson, M.; Vallin, K. S. A.; Wallner, O. A.; Hammarström, L. G. J.; Wüta, E.; Almlöf, I.; Kalderén, C.; Axelsson, H.; Djureinovic, T.; Puigvert, J. C.; Häggblad, M.; Jeppsson, F.; Martens, U.; Lundin, C.; Lundgren, B.; Granelli, I.; Jensen, A. J.; Artursson, P.; Nilsson, J. A.; Stenmark, P.; Scobie, M.; Berglund, U. W.; Helleday, T. MTH1 inhibition eradicates cancer by preventing sanitation of the dNTP pool. *Nature* **2014**, *508*, 215–221.
- Huber, K. V. M.; Salah, E.; Radic, B.; Gridling, M.; Elkins, J. M.; Stukalov, A.; Jemth, A.-S.; Göktürk, C.; Sanjiv, K.; Strömberg, K.; Pham, T.; Berglund, U. W.; Colinge, J.; Bennett, K. L.; Loizou, J. I.; Helleday, T.; Knapp, S.; Superti-Furga, G. Stereospecific targeting of MTH1 by (S)-crizotinib as an anticancer strategy. *Nature* **2014**, *508*, 222–227.
- Egashira, A.; Yamauchi, K.; Yoshiyama, K.; Kawate, H.; Katsuki, M.; Sekiguchi, M.; Sugimachi, K.; Maki, H.; Tsuzuki, T. Mutational specificity of mice defective in the MTH1 and/or the MSH2 genes. *DNA Repair* **2002**, *1*, 881–893.

(5) Kobold, S.; Wiedemann, G.; Rothenfuß, S.; Endres, S. Modes of action of TLR7 agonists in cancer therapy immunotherapy. *Immunotherapy* **2014**, *6*, 1085–1095.

(6) Raasch, B. Management of superficial basal cell carcinoma: focus on imiquimod. *Clin., Cosmet. Invest. Dermatol.* **2009**, *2*, 65–67.

(7) Greiff, L.; Cervin, A.; Ahlstrom-Emanuelsson, C.; Almqvist, G.; Andersson, M.; Dolata, J.; Eriksson, L.; Hoegestaett, E.; Kaellen, A.; Norlen, P.; Sjölin, L.-L.; Widegren, H. Repeated intranasal TLR7 stimulation reduces allergen responsiveness in allergic rhinitis. *Respir. Res.* **2012**, *13*, 53.

(8) Diebold, S. S. Recognition of viral single-stranded RNA by toll-like receptors. *Adv. Drug Delivery Rev.* **2008**, *60*, 813–823.

(9) Bonfanti, J.-F.; Fortin, J. M. C.; Muller, P.; Doublet, F. M. M.; Raboisson, P. J.-M. B.; Arnoult, E. P. A. Preparation of macrocyclic purines for the treatment of viral infections. *PCT Int. Appl. WO2014009509*, 2014.

(10) Meyer, T.; Surber, C.; French, L. E.; Stockfleth, E. Resiquimod, a topical drug for viral skin lesions and skin cancer. *Expert Opin. Invest. Drugs* **2013**, *22*, 149–159.

(11) Kurimoto, A.; Ogino, T.; Ichii, S.; Isobe, Y.; Tobe, M.; Ogita, H.; Takaku, H.; Sajiki, H.; Hirota, K.; Kawakami, H. Synthesis and evaluation of 2-substituted 8-hydroxyadenines as potent interferon inducers with improved oral bioavailabilities. *Bioorg. Med. Chem.* **2004**, *12*, 1091–1099.

(12) Kazaoka, K.; Sajiki, H.; Hirota, K. Synthesis of 6-substituted 9-benzyl-8-hydroxypurines with potential interferon-inducing activity. *Chem. Pharm. Bull.* **2003**, *51*, 608–611.

(13) Gerster, J. F.; Lindstrom, K. J.; Miller, R. L.; Tomai, M. A.; Birmachu, W.; Bomersine, S. N.; Gibson, S. J.; Imbertson, L. M.; Jacobson, J. R.; Knafla, R. T.; Maye, P. V.; Nikolaidis, N.; Oneyemi, F. Y.; Parkhurst, G. W.; Pecore, S. E.; Reiter, M. J.; Scribner, L. S.; Testerman, T. L.; Thompson, N. J.; Wagner, T. L.; Weeks, C. E.; Andre, J.-D.; Lagain, D.; Bastard, Y.; Lupu, M. Synthesis and structure-activity-relationships of 1H-imidazo[4,5-c]quinolines that induce interferon production. *J. Med. Chem.* **2005**, *48*, 3481–3491.

(14) Svensson, L. M.; Jemth, A. S.; Desroses, M.; Loseva, O.; Helleday, T.; Högbom, M.; Stenmark, P. Crystal structure of human MTH1 and the 8-oxo-dGMP product complex. *FEBS Lett.* **2011**, *585*, 2617–2621.

(15) Wei, T.; Gong, J.; Jamitzky, F.; Heckl, W. M.; Stark, R. W.; Rössle, S. C. Homology modeling of human toll-like receptors TLR7, 8, and 9 ligand-binding domains. *Protein Sci.* **2009**, *18*, 1684–1691.

(16) Molina, D. M.; Jafari, R.; Ignatashchenko, M.; Seki, T.; Larsson, E. A.; Dan, C.; Sreekumar, L.; Cao, Y.; Nordlund, P. Monitoring drug target engagement in cells and tissues using the cellular thermal shift assay. *Science* **2013**, *341*, 84–87.

(17) Persengiev, S. P.; Zhu, X.; Green, M. R. Nonspecific, concentration-dependent stimulation and repression of mammalian gene expression by small interfering RNAs (siRNAs). *RNA* **2004**, *10*, 12–18.

(18) Tarcsay, Á.; Keserű, G. M. Contributions of molecular properties to drug promiscuity. *J. Med. Chem.* **2013**, *56*, 1789–1795.

(19) Arrowsmith, C. H.; Audia, J. E.; Austin, C.; Baell, J.; Bennett, J.; Blagg, J.; Bountra, C.; Brennan, P. E.; Brown, P. J.; Bunnage, M. E.; Buser-Doepner, C.; Campbell, R. M.; Carter, A. J.; Cohen, P.; Copeland, R. A.; Cravatt, B.; Dahlin, J. L.; Dhanak, D.; Edwards, A. M.; Frederiksen, M.; Frye, S. V.; Gray, N.; Grimshaw, C. E.; Hepworth, D.; Howe, T.; Huber, K. V. M.; Jin, J.; Knapp, S.; Klotz, J. D.; Kruger, R. G.; Lowe, D.; Mader, M. M.; Marsden, B.; Mueller-Fahrnow, A.; Müller, S.; O'Hagan, R. C.; Overington, J. P.; Owen, D. R.; Rosenberg, S. H.; Ross, R.; Roth, B.; Schapira, M.; Schreiber, S. L.; Shoichet, B.; Sundström, M.; Superti-Furga, G.; Taunton, J.; Toledo-Sherman, L.; Walpole, C.; Walters, M. A.; Willson, T. M.; Workman, P.; Young, R. N.; Zuercher, W. J. The promise and peril of chemical probes. *Nat. Chem. Biol.* **2015**, *11*, 536–541.

(20) (a) Tajiri, T.; Maki, H.; Sekiguchi, M. Functional cooperation of MutT, MutM and MutY proteins in preventing mutations caused by spontaneous oxidation of guanine nucleotide in escherichia coli. *Mutat. Res., DNA Repair* **1995**, *336*, 257–267. (b) Rotman, E.; Kuzminov, A.

The *mutT* defect does not elevate chromosomal fragmentation in *Escherichia coli* because of the surprisingly low levels of MutM/MutY-recognized DNA modifications. *J. Bacteriol.* **2007**, *189*, 6976–6988.
(c) Tsuzuki, T.; Egashira, A.; Kura, S. Analysis of MTH1 gene function in mice with targeted mutagenesis. *Mutat. Res., Fundam. Mol. Mech. Mutagen.* **2001**, *477*, 71–78.